UNIVERSITY OF OKLAHOMA

GRADUATE COLLEGE

EXAMINING CERES DOWNWARD SHORTWAVE SURFACE RADIATIVE FLUX MEASUREMENTS IN THE CONTEXT OF OKLAHOMA MESONET MEASUREMENTS IN 2019-2021

A THESIS

SUBMITTED TO THE GRADUATE FACULTY

in partial fulfillment of the requirements for the

Degree of

MASTER OF SCIENCE

By

BRADLEY FLETCHER LAMKIN

Norman, Oklahoma

2023

EXAMINING CERES DOWNWARD SHORTWAVE SURFACE RADIATIVE FLUX MEASUREMENTS IN THE CONTEXT OF OKLAHOMA MESONET MEASUREMENTS IN 2019-2021

A THESIS APPROVED FOR THE
SCHOOL OF METEOROLOGY

BY THE COMMITTEE CONSISTING OF

Dr. Jens Redemann, Chair

Dr. Feng Xu

Dr. Ian Chang

Acknowledgments

Wow! The last two years have genuinely been memorable and amazing. My time at OU has been a fantastic journey. There have been so many people in the past two years that have supported me; where do I even begin?

First, I want to thank my advisor, Jens Redemann. When I applied to the School of Meteorology, I worked on creating flash flood and severe weather days 3-7 risk algorithms with the National Weather Service Baltimore/Washington Office. During my Senior year at Virginia Tech, I worked with Dr. Craig Ramseyer on studying atmospheric rivers in the Mid-Atlantic. So, you can imagine my surprise when I got interviewed by Jens. The interview was special, and I knew he was the right advisor for me from that moment. He listened to my concerns, emphasized the importance of work-life balance, and was instrumental in my learning about aerosol-cloud-radiation interactions. Thank you, Jens, for everything, and I know we will be long-term friends after completing my graduate studies.

I would also like to thank Dr. Ian Chang for giving me excellent advice and feedback on my work. He repeatedly told me, "treat your thesis like a tennis match." This resonated with me as a tennis player. Also, I would like to thank all of my other colleagues in the $(CL)^2$EAR research group: Dr. Connor Flynn, Dr. Lan Gao, Abdulamid Fakoya, Logan Mitchell, and Emily Lenhardt. Their support, kindness, and motivation have made group meetings, conferences, and social gatherings much more enjoyable. I would also like to thank Dr. Feng Xu for serving on my committee and providing excellent radiative transfer feedback. Also, I would like to thank Dr. Jason Furtado for being my go-to for statistics questions. I would also like to thank the Meteorology faculty at Virginia Tech: Dr. Craig Ramseyer, Dr. Drew Ellis, Dr. Stephanie Zick, and Dave Carroll. Your encouragement and motivation helped get me to this point today!

Also, I want to thank my friends at OU: Connor Bruce, Drew Shearer, Saurabh Patil, Jake Margraf, Elizabeth Spicer, Andrew Messersmith, Jamilynne Johnson, and Matthew Bray. These people were always there for me and encouraged me to succeed.

Thanks for the fun memories that I will cherish forever. I would also like to thank my closest friends from Virginia Tech: Ryan Holgerson, Mark Skaggs, Levi Cornett, Alex Shevalier, Tyler McCormick, Cassie Belcher, Ben Sheppard, and Josh Haueis. The four years at Virginia Tech were the best four years of my life. Thanks for being lifelong friends and holding a special place in my heart. I would also like to thank my swim coach, Chris Hinton, for always encouraging me to be myself and to have fun. Thanks for being a significant role model to me.

Finally, I would like to thank my parents, Barbara and Griffin Lamkin. They gave me lots of love and supported me throughout my collegiate journey. I could not have done this without them. Thanks a million!

I hope you enjoy reading this thesis as much as I enjoyed writing it. Thanks for everything!

Table of Contents

List Of Tables

List Of Figures

Abstract

The surface radiation budget affects different components of Earth's climate system. Accurate assessments of the surface radiation budget help improve climate forecasts, such as drought prediction. In addition, short-term diabatic heating and cooling influence convection, temperature, and wind. Surface observations are the most accurate way to measure surface radiative fluxes. However, many locations across the globe do not have access to precise surface radiation measurements. In addition, surface observations are point-based measurements and offer little spatial coverage. As a result, areas with little to no surface observations rely on top-of-the-atmosphere (TOA) satellite instruments to measure surface radiation. Accurate radiative flux measurements from space are much more complicated and prone to errors than surface observations as they are derived from TOA radiances. Thus, a thorough understanding of satellite-based surface flux data are needed.

The Clouds and the Earth's Radiant Energy System (CERES) is an instrument currently deployed on four satellites. Surface radiative fluxes derived from CERES TOA measurements must account for atmospheric variables such as aerosol optical depth, zenith angle, aerosol and trace gas concentrations, cloud fraction, cloud optical thickness, and cloud albedo. The State of Oklahoma invested in a dense Mesonet network of 120 stations. A dense population of Mesonet stations with a high-resolution product makes it possible to effectively evaluate the CERES surface downward shortwave radiative fluxes based on a simple parameterized code.

This work compares the CERES-Aqua and CERES-Terra Single Scanner Footprint (SSF) Level 2 Edition 4A surface radiation product collocated with the Mesonet-derived observed downward shortwave radiative fluxes for the period 2019 to 2021. We explore clear-sky and all-sky environments by separating the dataset into three different bins using the Moderate Resolution Imaging Spectrometer (MODIS). We find a strong correlation (i.e., correlation coefficient greater than 0.9) between CERES-Aqua and CERES-Terra downward shortwave surface radiative fluxes with the collocated equivalent Mesonet irradiance observations for all three cloud fraction bins.

The correlation coefficients of the all-sky bins slightly increased versus the clear-sky bins. During all three years, the CERES-Terra data had higher Mean Absolute Difference (MAD), Mean Bias Difference (MBD), and Root Mean Squared Difference (RMS) than the CERES-Aqua data. We also examine the seasonal dependence of the CERES-Mesonet differences, where the summer all-sky differences are larger than the other seasons.

Chapter 1

Background and Introduction

1.1 Atmospheric Radiation

Energy is the ability to do work on an element of mass (Ahrens 2016). Radiation is the thermal energy transfer from one substance through space. Atmospheric radiation travels through Electromagnetic (EM) waves in the direction orthogonal to the electric and magnetic fields (Figure 1.1) (Petty 2006).

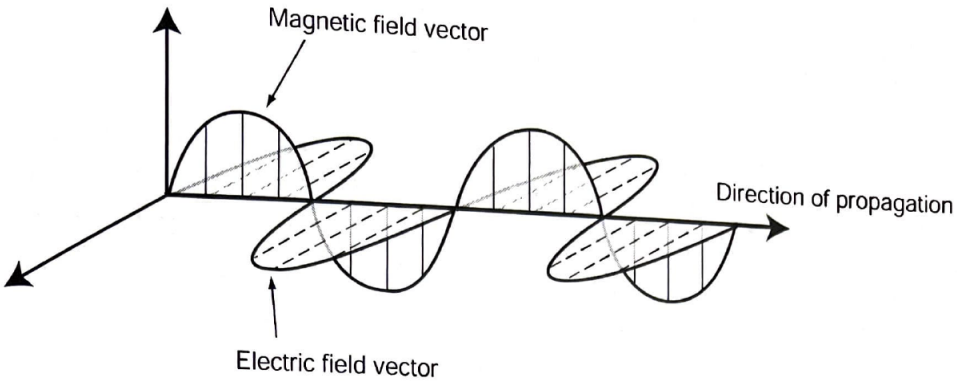

Figure 1.1: Schematic from Petty (2006), the direction of the electric field, magnetic field, and wave propagation on the x, y, z plane.

Convection, sensible heat processes, climate feedbacks, the hydrological cycle, snow melt, and the Greenhouse Effect are all driven at least in part by atmospheric radiation (Chakraborty and Lee 2021). The wavelength of EM waves is defined as the

distance between two crests (Ahrens 2016). Ahrens also defines the EM Spectrum as classifying spectral bands based on their wavelengths (Figure 1.2).

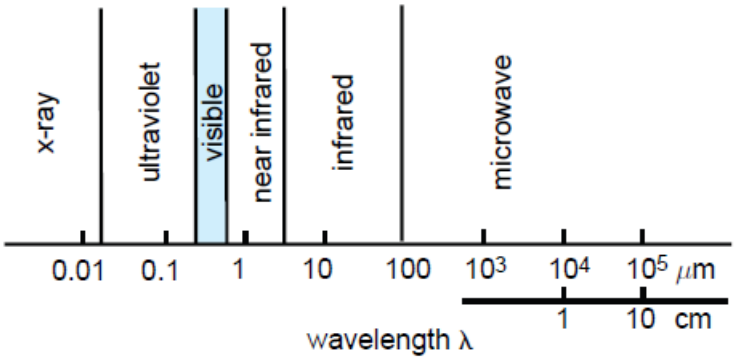

Figure 1.2: Schematic from Wallace and Hobbs (2006), the full Electromagnetic Spectrum.

The solar zenith angle (θ) is the angle of the incoming solar radiation, relative to the **k** unit vector (Petty 2006). The solar azimuth angle (φ) is counterclockwise from a reference point in the horizon on the x, y plane. The solid angle (ω) is defined as the three-dimensional area formed by a conical area (Figure 1.3).

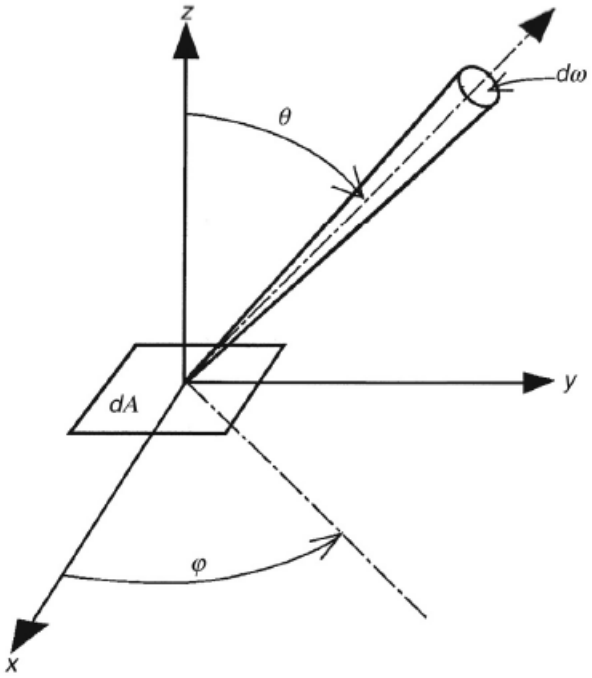

Figure 1.3: The relationship between the solar zenith angle (θ), azimuth angle (φ), and solid angle (ω) (Hartmann 2016).

The spectral radiance (I_λ) is defined as the incoming EM radiation from a specific direction per unit time per unit area at a given wavelength (Wallace and Hobbs 2006). Radiance (I) is the integration of the spectral radiances over a given spectral band

$$I = \int_{\lambda_1}^{\lambda_2} I_\lambda d\lambda \tag{1.1}$$

where λ_1 and λ_2 are the lower and upper wavelengths of the spectral band, respectively. Irradiance, or flux density (F), is the power measurement per unit area (Kato

et al. 2018). It is calculated by integrating the radiance times the cosine of the zenith angle over a given solid angle.

$$F = \int_{2\pi} I \cos\theta d\omega \tag{1.2}$$

A blackbody is a surface that absorbs all incoming solar radiation (Wallace and Hobbs 2006). In the atmosphere, the constituents do not absorb all solar radiation, but using an idealized blackbody model can help understand the emission of radiation by different sources. The Planck Function describes the radiation emitted by a blackbody (B_λ) as a function of temperature (T) and wavelength (λ) (Wallace and Hobbs 2006).

$$B_\lambda = \frac{c_1 \lambda^{-5}}{\pi \left(e^{\frac{c_2}{\lambda T}} - 1 \right)} \tag{1.3}$$

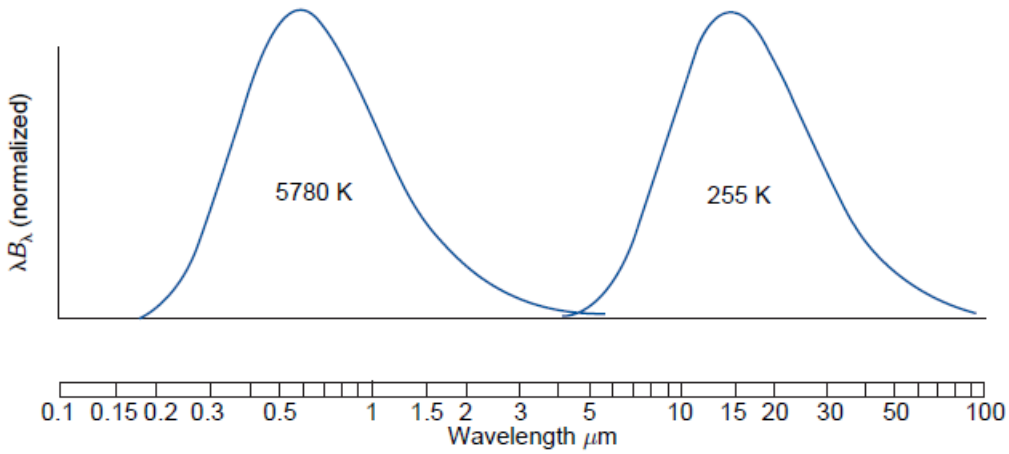

Figure 1.4: Planck Curves for the Sun (left side) and the Earth (right side) (Wallace and Hobbs 2006; Goody and Yung 1995).

The Planck curves show the emission of blackbody radiation by the sun and Earth at given temperatures (Figure 1.4). Wein's Displacement Law describes the relationship between the temperature and wavelength of a blackbody. Wien's Displacement Law describes that the maximum emitted wavelengths are inversely proportional to the temperature of the blackbody. (Wallace and Hobbs 2006). Since the Sun is much warmer than the Earth, the Sun's maximum emission is at shorter wavelengths. Therefore, we classify emitted solar radiation as shortwave and emitted terrestrial radiation as longwave.

1.2 Surface Radiation Budget

The global energy budget is an essential component of the Earth-atmosphere system, as it is one of the unique aspects of Earth that allows for life (Wallace and Hobbs 2006). In a balanced Earth, the energy received by the Earth should be approximately equal to the energy outgoing (Forster et al. 2021; Brown et al. 2014). The surface radiation budget also influences hydrologic and oceanic processes (Forster et al. 2021). There are significant differences between cloud-free conditions and atmospheric conditions in the presence of clouds. Clouds are critical contributors to the scattering and absorption of atmospheric radiation (Lenhardt et al. 2023). As a result of the changes to the surface radiation budget as a consequence of clouds, it is paramount to study the surface radiation budget in both all-sky and clear-sky conditions.

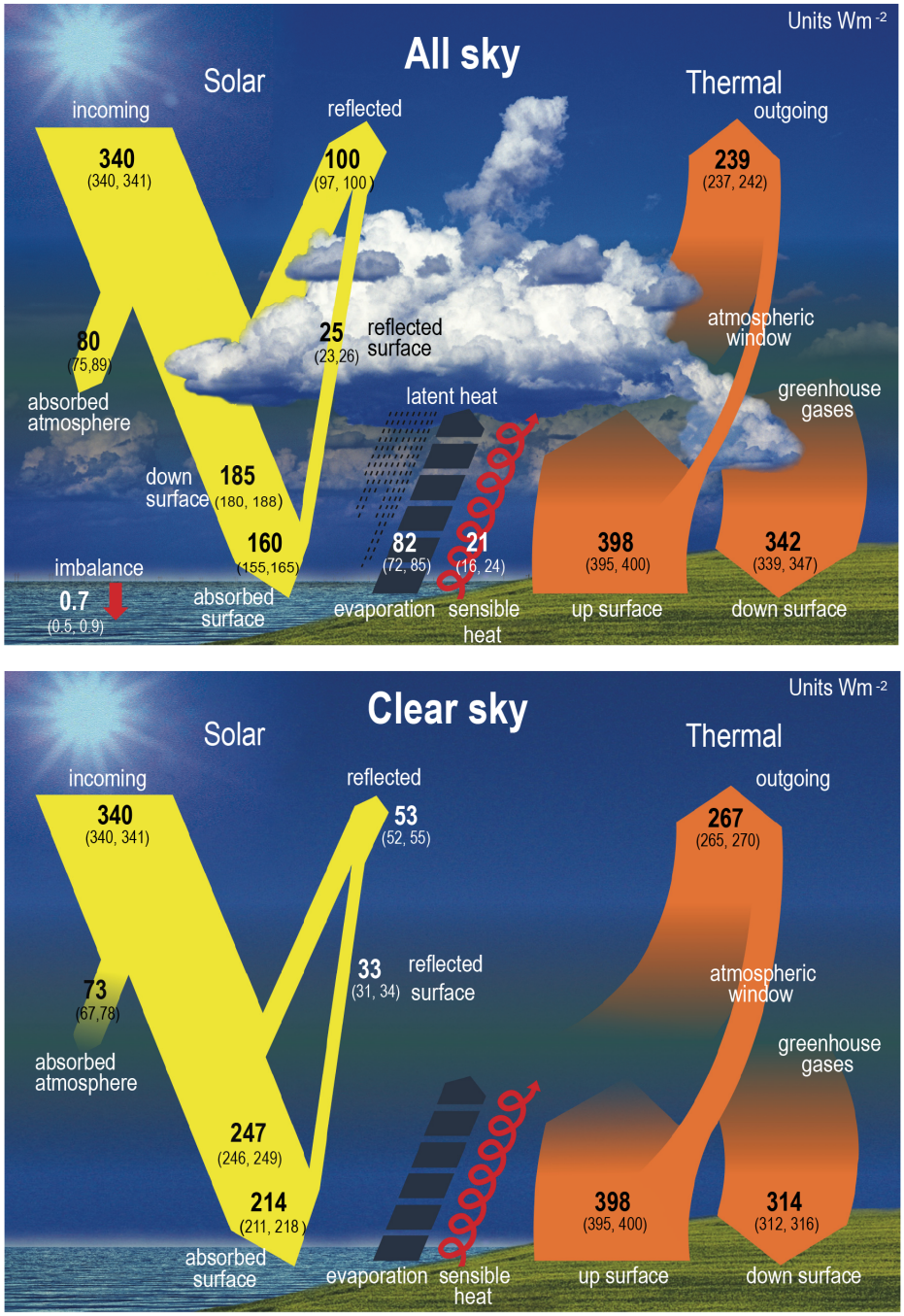

Figure 1.5: Global radiation budget for all-sky (top panel) and clear-sky (bottom panel) atmospheres. Numbers indicate globally averaged radiative fluxes with 95% confidence interval in parentheses (Forster et al. 2021; Wild et al. 2015).

The schematic above is the global averaged radiation budget at 2000 (Figure 1.5). In clear-sky conditions, more shortwave radiation reaches the surface, and less shortwave and longwave radiation is reflected to space (Forster et al. 2021; Wild et al. 2015). Since there is a top-of-the-atmosphere (TOA) radiation imbalance under clear-sky conditions, the Earth would be significantly warmer without the presence of clouds. While we mostly understand the TOA radiation budget, the surface radiation budget has much more uncertainty (Forster et al. 2021; Kato et al. 2018; Kratz et al. 2010). Regional surface radiative budget analysis has even more uncertainties due to the deficiency of surface observations. As a result, there are many uncertainties with the regional surface radiative budget, and this project works to ameliorate our understanding of these uncertainties.

1.3 Atmospheric Aerosols

Atmospheric aerosols are small particles suspended in the air (Wallace and Hobbs 2006). Particle sizes vary from Aiken nuclei (0.001 μm-0.1 μm), large particles (0.1 μm-5 μm), and giant particles (5 μm-100 μm) (Wallace and Hobbs 2006). Some aerosols are naturally occurring, and others are anthropogenic. Anthropogenic aerosols are important drivers of climate change and have a high degree of uncertainty (Redemann et al. 2021). The Intergovernmental Panel on Climate Change (IPCC) is interested in studying anthropogenic aerosols as their emissions can be controlled by government intervention (Forster et al. 2021).

To understand how aerosols impact the climate, radiative forcing, cloud development, and human health, determining aerosol composition is essential. Anthropogenic

aerosols can be broadly placed into four categories: sulfates, carbons, dust, and sea salt (Ramanathan et al. 2001).

Aerosols scatter (to space or other parts of the atmosphere), absorb, or transmit solar radiation. The sum of the scattering and absorption of solar radiation is known as extinction. The aerosol extinction coefficient ($\beta_{e,\text{aerosol}}$) is a mathematical representation of the amount of solar radiation scattered and absorbed by the aerosol (Petty 2006). The Aerosol Optical Depth (AOD; $\tau_{aerosol}$) measures the optical thickness as a result of aerosol extinction (Wallace and Hobbs 2006). It is calculated by integrating the aerosol extinction coefficient over a vertical layer

$$\tau_{\text{aerosol}} = \int_{s_1}^{s_2} \beta_{e,\text{aerosol}} ds \tag{1.4}$$

where s_1 and s_2 are the lower and upper altitudes of the layer. Studying AOD will help determine which regions have the most aerosol loading.

1.4 Aerosol-Cloud-Radiation Interactions

1.4.1 Aerosol-Radiation Interactions

Aerosols and radiation interactions have profound impacts on the global and regional climate. The amount of radiation scattered and absorbed by aerosols depends on their size, chemical composition, and optical properties (Petty 2006). A decrease in downwelling irradiance is expected as a fraction of the incoming solar radiation is scattered back toward the TOA as cloud cover and aerosol concentration increase. (Xie and Liu 2013). Aerosols disperse a fraction of shortwave irradiance back to space, which leads to a net cooling effect (Forster et al. 2021). On the other hand,

there will be a local warming effect due to sensible heating in the aerosol layer for absorbing aerosols. Below the aerosol layer, less solar radiation reaches the surface locally, as more radiation is attenuated.

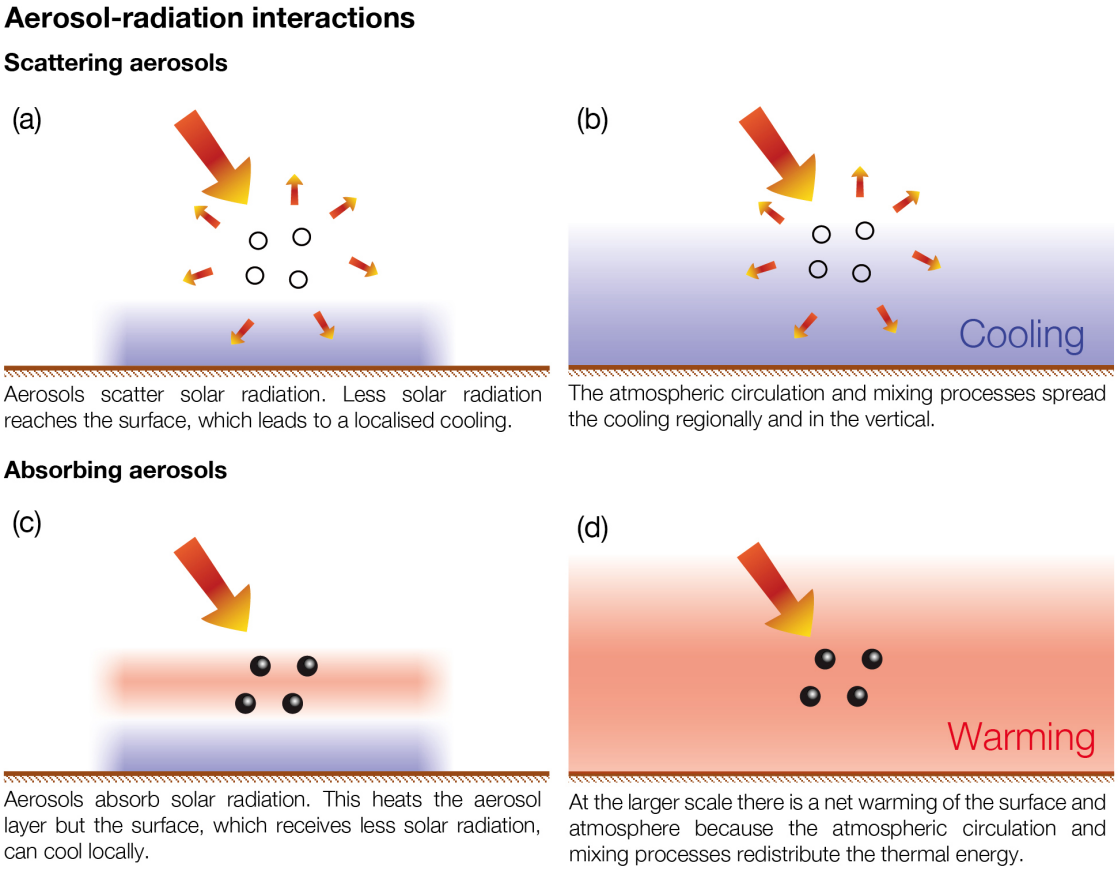

Figure 1.6: Scattering aerosols (a) locally and (b) regionally, and absorbing aerosols (c) locally and (d) regionally (Stocker et al. 2013).

On a regional scale, scattering aerosols extend a net cooling effect spatially due to atmospheric circulation and mixing (Forster et al. 2021). However, there is a net warming effect regionally at the surface and atmosphere for absorbing aerosols as thermal energy is redistributed through mixing and the general circulation (Figure 1.6).

Most atmospheric aerosols lie within the Mie scattering regime. Thus, most radiation is scattered forward, while little is scattered elsewhere (Ensor et al. 1971; Budyko 1969). Direct radiative forcing is defined as the changes to the climate resulting from aerosol extinction (Ramanathan et al. 2001). The indirect radiative effects are the increases in droplet number concentration due to more aerosols and the increase in cloud fraction due to aerosol-induced effects on cloud lifetime. Understanding the aerosol direct and indirect effects will result in a better understanding of regional climate and weather processes.

1.4.2 Aerosol-Cloud Interactions

Aerosol-cloud interactions have a large degree of uncertainty due to the complex processes involved and the lack of understanding of the governing physics. Furthermore, aerosols are spatially and temporally heterogeneous due to variations in aerosol sources (Redemann et al. 2021). Aerosols form the basis of CCN; therefore, the cloud drop number concentration increases are proportional to increases in CCN for some clouds (Figure 1.7) (Twomey 1959; Forster et al. 2021).

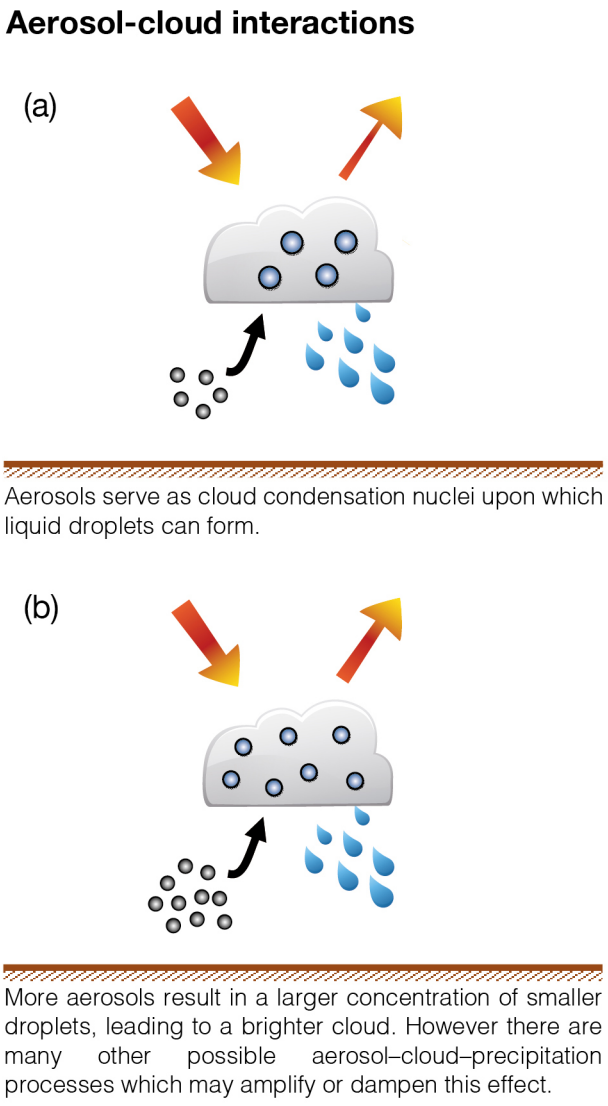

Figure 1.7: (a) CCN forming from aerosols, which are the basis for cloud droplets; (b) aerosols are proportional to the amount of solar radiation reflected (Stocker et al. 2013).

Effective radiative forcing (ERF) is the combined radiative effects of the tropospheric land and surface changes and stratospheric temperature changes (Smith et al. 2018). The instantaneous radiative forcing (IRF) is the sum of the cloud-albedo and

aerosol effects (Smith et al. 2018). ERF is calculated using Eq. (1.5) (Smith et al. 2018; Chung and Soden 2015)

$$\text{ERF} = \text{IRF} + A_T + A_{T_s} + A_q + A_\alpha + A_c + \epsilon \tag{1.5}$$

where "A_x is the rapid adjustment x due to atmospheric temperature (T), surface temperature (T_s), water vapor (q), surface albedo (α), and clouds (c)" (Smith et al. 2018). Assuming a constant liquid water content as cloud effective radius decreases, cloud albedo increases, which induces negative surface radiative forcing (Forster et al. 2021).

Since the IPCC AR5 report, the AR6 report note significant progress in aerosol remote sensing (Forster et al. 2021). Despite progress, considerable uncertainty exists in evaluating the effect of aerosol-cloud interactions on ERF. Aerosol-cloud interactions have the largest amount of error since 1750 of -1.45 to -0.25 Wm^{-2} (Figure 1.8) (Forster et al. 2021). Due to the large uncertainties on how aerosol-cloud interactions affect ERF, it is important to learn about the distribution of aerosol chemical compositions, sizes, and types across the globe (Lohmann and Feichter 2005; Lenhardt et al. 2021). Performing regional radiative transfer analysis will help understand local aerosol-cloud interactions and improve climate modeling.

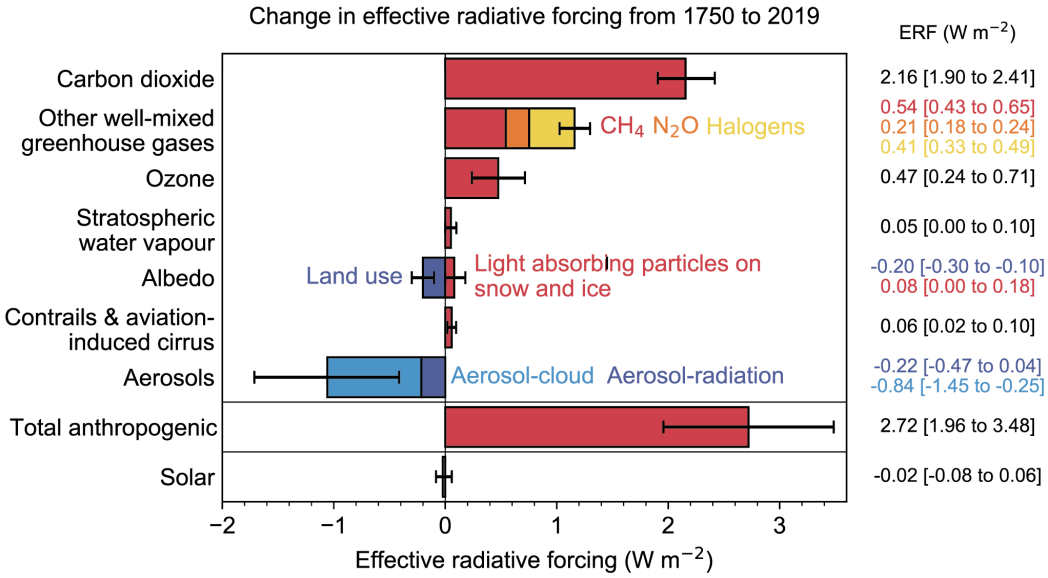

Figure 1.8: Contribution of different atmospheric constitutions from 1750 to 2019. Blacks lines are error bars (Forster et al. 2021).

1.5 Oklahoma Geography and Climate

Oklahoma was chosen due to its dense surface Mesonet network, of which all locations contain pyranometers. The nine unique climate zones offer an opportunity to examine which atmospheric system components affect the differences between surface observations and satellite-based measurements. Before the 1950s, the climate zones were primarily based on topography, land use and land cover, river districts, forecast areas of responsibility, and drainage basins (Guttman and Quayle 1996). After the 1950s, climatological variables were considered, with a reliable dataset beginning in the mid-1980s (Guttman and Quayle 1996). Temperature, precipitation, and heating/cooling degree days are all considered when determining climatic zones (Figure 1.9) (Guttman and Quayle 1996).

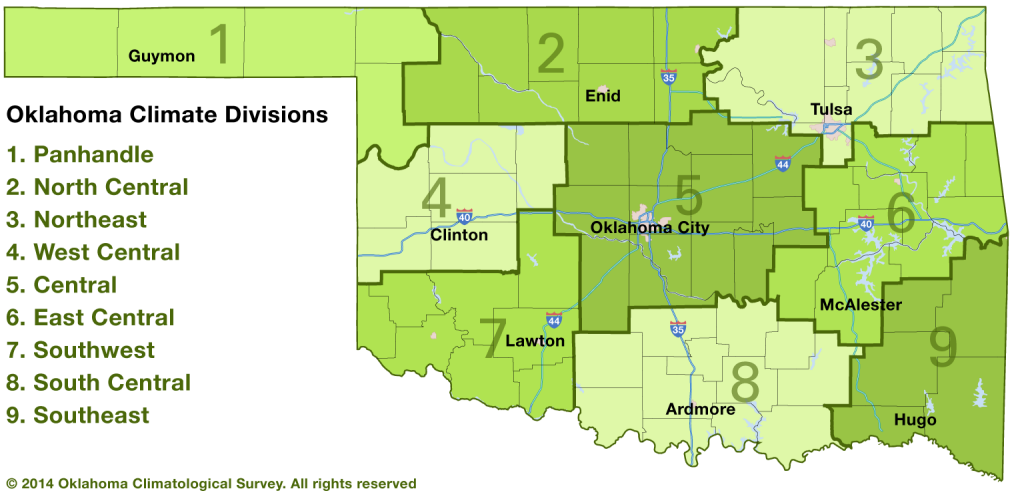

Figure 1.9: Oklahoma Climate Divisions defined from Guttman and Quayle (1996). Figure produced by the Oklahoma Climatological Survey (McPherson et al. 2007; Brock et al. 1995)

Understanding the regional differences in the radiation budget is important because it affects geophysical variables, such as soil moisture, which has large implications for the local economy. These include cash crops, such as wheat production (Illston et al. 2004; Zhang and Nearing 2005). Furthermore, the state has a diverse land use and land cover, with the eastern portion consisting of forested areas and the western portions featuring mainly cropland and grasslands (Figure 1.10) (Dewitz 2021).

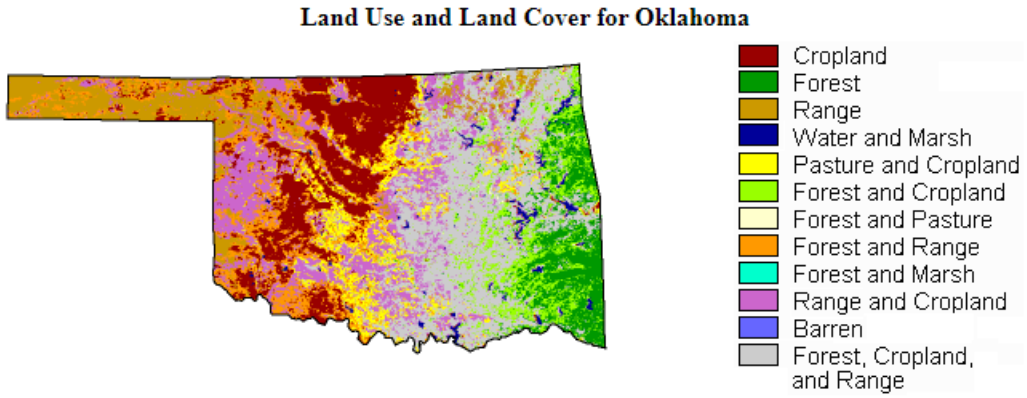

Figure 1.10: Land use and land cover map from the United States Geological Survey (Scott et al. 2000).

As with the land use and land cover distribution across Oklahoma, the precipitation and temperature magnitudes are strongly regional dependant. The eastern portions of the state average approximately 50 in of liquid equivalent precipitation a year, while western edges of the Panhandle average about 15 in of precipitation annually (Figure 1.11) (McPherson et al. 2007; Brock et al. 1995). Therefore, the eastern portions of the state average over three times more precipitation than the panhandle. This has enormous implications on land use and land cover, temperature distribution, and radiative effects. While the precipitation distribution is longitudinally dependent, the temperature distribution of Oklahoma is latitudinally dependent. The annual mean temperatures are coolest in the panhandle due to less latent heat release and warmest across the southern tier of the state (Figure 1.12) (McPherson et al. 2007; Brock et al. 1995). The mean annual temperature difference from the southern tier of Oklahoma to the panhandle (in °F) is approximately five to seven degrees (McPherson et al. 2007; Brock et al. 1995). An annual difference of even a few degrees Fahrenheit greatly affects the climate system. As a result of the discrepancy of climate regimes in Oklahoma, understanding the regional differences in

gaseous properties and their impacts on the radiation balance in Oklahoma are key components of this work.

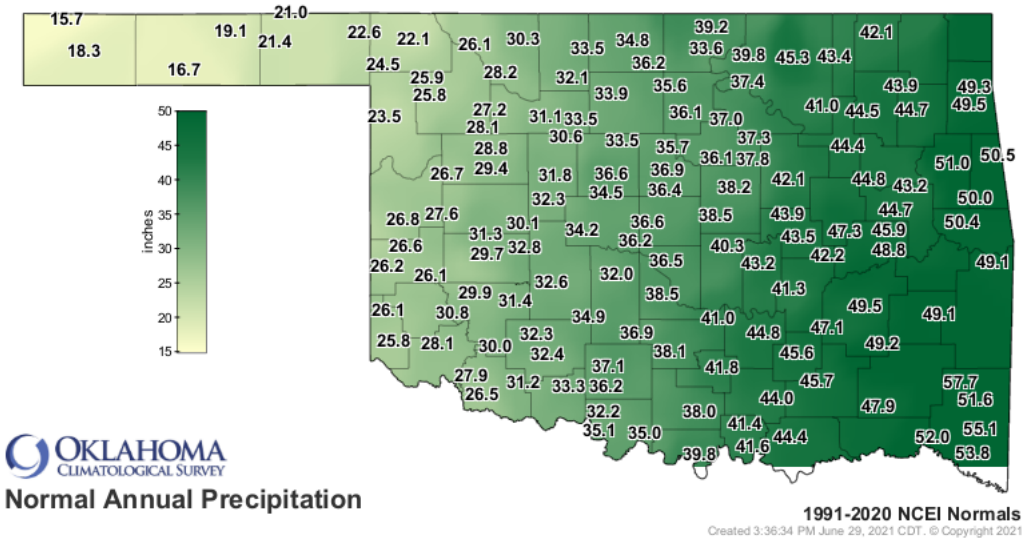

Figure 1.11: Average annual precipitation (in) from NCEI. Figure produced by the Oklahoma Climatological Survey (McPherson et al. 2007; Brock et al. 1995).

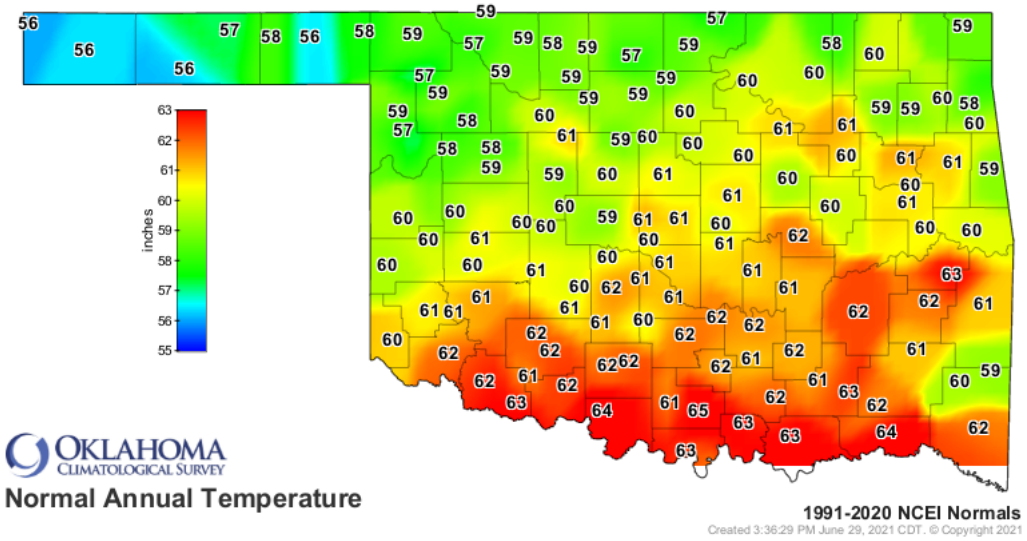

Figure 1.12: Average annual temperature (°F) from NCEI. Figure produced by the Oklahoma Climatological Survey (McPherson et al. 2007; Brock et al. 1995).

1.6 Project Goals and Scientific Significance

1.6.1 Project Goals

While ground-based radiation measurements are direct observations and less error-prone, they are too costly to maintain a dense global network of radiation instruments. Many locations across the globe do not have access to accurate surface radiation measurements. We rely on remote sensing instruments to observe their radiative budget from the TOA. Precise radiative flux measurements from remote sensing are much more complicated and prone to error than surface observations. Clouds and the Earth's Radiant Energy System (CERES) is an instrument currently deployed on four satellites. The device measures TOA radiances and converts them into surface irradiances using angular distribution models and simple parameterized code (Kratz et al. 2020; Loeb et al. 2016; Wielicki et al. 1996).

Oklahoma invested in a dense Mesonet network of 120 stations across the entire state (McPherson et al. 2007; Brock et al. 1995). A dense population of Mesonet stations within a region with diverse climate zones and reliable statistics makes it viable to effectively evaluate the CERES surface downward shortwave radiative flux simple parameterized code.

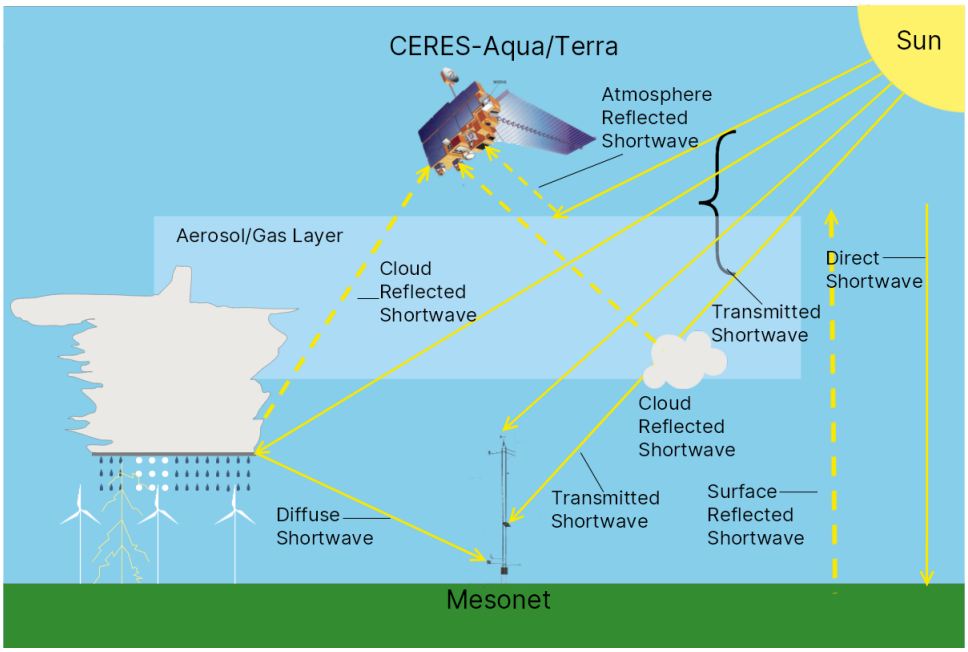

Figure 1.13: Schematic of shortwave radiative transfer theory relative to instrumentation used in this study.

This project aims to evaluate CERES downward shortwave radiative flux measurements, in which atmospheric properties are possible sources for errors in either the CERES or Mesonet products (Figure 1.13). This work uses CERES-Aqua and CERES-Terra surface radiation products collocated with the Mesonet-derived observed downward shortwave radiative fluxes from 2019 to 2021. Both clear-sky and all-sky filtering will be used to determine the contribution of clouds to the error and uncertainty.

1.6.2 Scientific Importance

This project provides a regional evaluation of the CERES-derived surface radiation product using a densely populated network of well-calibrated surface pyranometers

in multiple regional climate regimes. We can to scrutinize the regional differences and suggest which properties are possible explanations for larger CERES-Mesonet differences. In addition, this work can be conveyed to the CERES and Mesonet teams to inform them of any adjustments that need to be made to their products. After evaluating the radiative fluxes, studies to improve the ability to study Earth's radiation budget from space with critical links to dynamics and the hydrologic cycle are possible.

1.6.3 Science Questions

This project aimed to understand the strengths and limitations of the CERES product using ground-based measurements. The following science questions are addressed:

1. How well do CERES- and OK Mesonet-derived downwelling solar irradiances at the surface compare in 2019-2021?

2. Are there spatial and seasonal patterns to differences between CERES- and Mesonet-derived surface irradiances?

3. Are the spatiotemporal patterns attributable to specific cloud types?

Chapter 2

Data & Methods

2.1 Datasets and Instrumentation

2.1.1 Oklahoma Mesonet

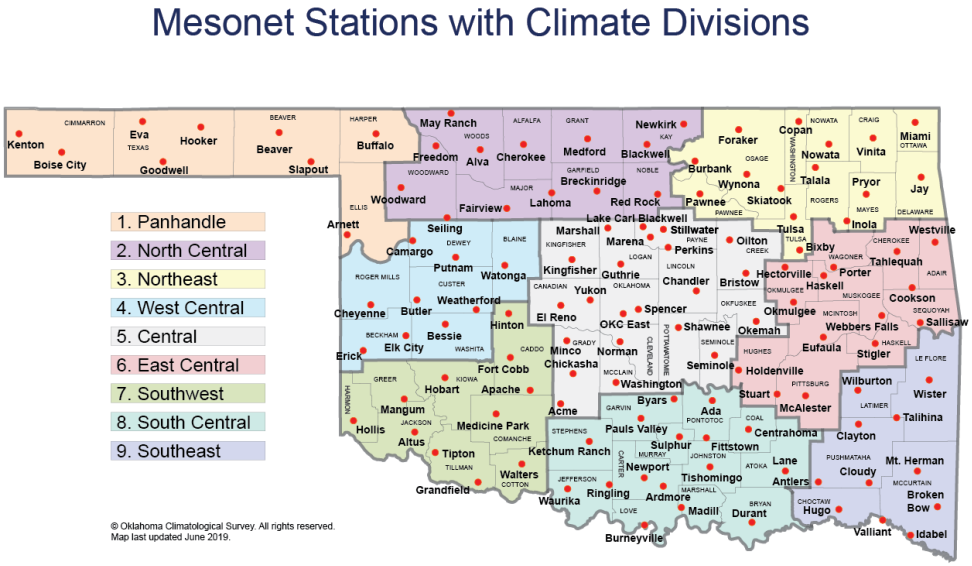

Figure 2.1: Oklahoma Mesonet stations map overlaid with climate divisions (McPherson et al. 2007; Brock et al. 1995; Guttman and Quayle 1996).

The Oklahoma Mesonet is a weather station network currently containing 120 stations across Oklahoma (McPherson et al. 2007; Brock et al. 1995). The distribution of the Mesonet stations is heterogeneous, with more stations concentrated over

population centers and fewer stations in the panhandle (Figure 2.1). The Mesonet Li-Cor pyranometers undergo a rigorous quality assurance assessment to ensure accuracy (Shafer et al. 2000). The sensors are calibrated indoors as necessary at the Kipp and Zonen Calibration Facility and only take a few minutes (McPherson et al. 2007). The instruments are mounted 1.5 m above ground level and are on a beam along the tower's southern part to avoid lightning damage (Figure 2.2) (McPherson et al. 2007).

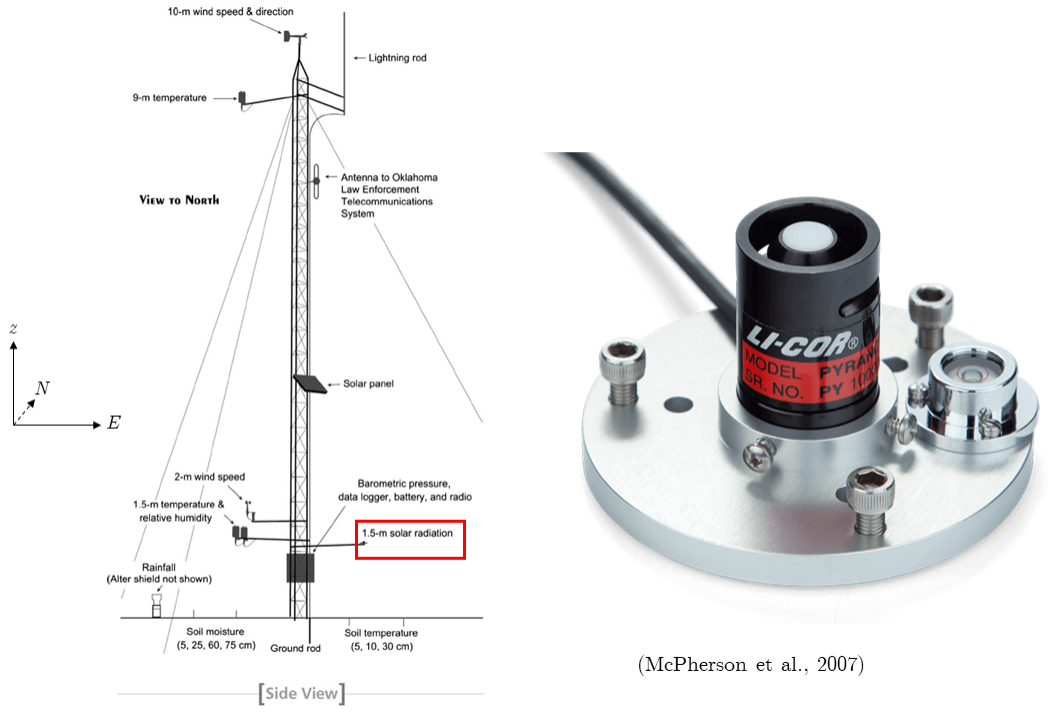

(McPherson et al., 2007)

Figure 2.2: Side view of an Oklahoma Mesonet station with a zoomed-in image of the LI-COR pyranometer on the right (McPherson et al. 2007).

The specific pyranometers used on the station are LI-COR LI-200R series (McPherson et al. 2007). These instruments must be used outdoors and require unblocked direct sunlight (McCree 2022). The LI-200R pyranometers measure total (diffuse plus direct) incoming shortwave irradiances. Their spectral range is between 400-1100 nm.

In addition, the pyranometer uses an unfiltered silicon photodiode and is corrected for cosine-dependent measurement errors. Accuracy estimates apply to data collected for incident angles up to 82°, beyond which the instrument response function and surface reflections and obstructions become non-negligible contributions to measurement uncertainty.

2.1.2 Clouds and the Earth's Radiant Energy System

Clouds and the Earth's Radiant Energy System (CERES) instruments measure TOA radiances in three spectral bands: 0.2-100 μm, 0.2-5 μm, and 8-12 μm (Kratz et al. 2010). After integrating the radiances with angular distribution models, the irradiances are gridded and time-averaged. The Single Scanner Footprint (SSF) Edition 4A product uses a simple parameterization to calculate the surface shortwave irradiances. The spatial resolution is 20 km at the nadir and up to 50 km at the swath edges (Kratz et al. 2020). The downward shortwave surface radiative flux (F_0) is calculated by

$$F_0 = \underbrace{S_0 \mu d^{-2}}_{①} \underbrace{T_a}_{②} \underbrace{T_c}_{③} \tag{2.1}$$

with S_0 equalling the solar constant, d equalling the earth-sun distance, μ equalling the cosine of the solar zenith angle, T_a equalling the atmospheric transmission of a clear-sky atmosphere, and T_c equalling the transmittance by clouds (Kratz et al. 2020). Term ① represents the inverse square law, which describes that the total radiation emitted from the sun is inversely proportional to the distance squared. Term ② represents the atmospheric transmission using a variation of Beer-Lambert's Law

$$T_a = (1 + B) \exp(-\tau_z) \tag{2.2}$$

where B is the scattering of trace gasses and aerosols and τ_z is the extinction optical depth (Kratz et al. 2010). Finally, term (3) represents the cloud transmittance, which was empirically derived by Darnell et al. (1992) as

$$T_c = 0.05 + 0.95 \left(\frac{R_{ovc} - T_{meas}}{R_{ovc} - R_{clr}} \right) \tag{2.3}$$

where R_{ovc} is the overcast TOA reflectance, R_{clr} is the TOA clear-sky reflectance, and R_{meas} is the TOA measured reflectance by CERES (Darnell et al. 1992; Kratz et al. 2010). While a version of the instrument is deployed on four satellites, we only use Terra and Aqua here. We chose Terra and Aqua due to their longer, more comprehensive data record than the Suomi NPP and NOAA-20 satellites. Terra and Aqua are polar-orbiting satellites that view Oklahoma approximately once per day during the daylight hours, which are 10:30 AM and 1:30 PM for Terra and Aqua, respectively (Kato et al. 2013).

2.1.3 Moderate Resolution Imaging Cloud Spectrometer

The Moderate Resolution Imaging Spectroradiometer (MODIS) imagers, which also operate on Aqua and Terra, cover most mid-latitude regions twice daily, day and night. We use cloud and aerosol products derived from MODIS radiances within the CERES footprint to provide insights on which constituents the CERES simple parameterized code might not correctly account for. How CERES accounts for cloud properties is a crucial source of uncertainty (Kato et al. 2013). Aerosol optical depth, cloud top height, and cloud fraction are all used to evaluate how CERES performs under specific background environments.

2.2 Collocation of Mesonet and Satellite Instruments

The Oklahoma Mesonet and CERES have two completely different methods of observation. The Oklahoma Mesonet stations are stationary, and the pyranometers collect total incoming shortwave radiation measurements every 5 seconds (McPherson et al. 2007; Brock et al. 1995; Illston et al. 2004). These observations are ground-based "point" observations with exact latitudes and longitudes. On the other hand, CERES shortwave surface radiative flux measurements only occur once per day per satellite. In addition, the measurements are part of a swath, with a 20 km spatial resolution near the nadir and a 50 km spatial resolution near the swath edges. Therefore, the collocation with Mesonet was with the CERES swaths latitude and longitude centroids.

Since the CERES measurements are not exactly at the same time each day, and Mesonet only measures irradiances every five minutes, each measurement was assigned to the nearest five minutes. For example, a CERES-Terra overpass time of 10:33 AM would be rounded to 10:35 AM, and a CERES-Aqua measurement at 1:32 PM would be rounded to 1:30 PM. After rounding, the great circle distance (d) from each CERES measurement to the fixed Mesonet station was calculated using the Haversine Formula (Chopde and Nichat 2013).

2.3 Cloud Fraction Categories

We looked at cloud-free versus cloudy cases to evaluate how the CERES product performed in a simpler framework. To identify clear-sky cases, we used the cloud

fraction product derived from MODIS radiances and collocated within the CERES footprint. We defined clear-sky cases as cloud fractions less than or equal to 5% based on Kato et al. (2018) study. All-sky encompassed all cases, regardless of the cloud fraction. Most statistical techniques discussed in section 2.4 were studied under all-sky and clear-sky cases.

2.4 Statistical Methods

After collocating CERES-Terra and CERES-Aqua measurements with Mesonet observations and applying filtering for clear-sky conditions, we created regular and density-gradient scatterplots to determine where outliers were clustered. Furthermore, we used ordinary least squares (OLS) linear regression to calculate the line-of-best fit. Since both sensors measure the surface shortwave irradiances at approximately the same longitude and latitude, an OLS close to the unity line indicates excellent agreement between the two sensors. The strength of the linear relationship was determined by calculating Pearson's Correlation Coefficient (Isaac 2018). We calculated Spearman's Rank Correlation Coefficient to establish the general relationship between CERES-Terra/Aqua and Mesonet at Terra/Aqua overpass times (Schober et al. 2018). Root mean squared differences (RMS), mean bias differences (MBD), and mean absolute differences (MAD) were used to determine the average magnitude and bias of the error (Chai and Draxler 2014). All correlation values are dimensionless, and error values are reported in watts per square meter (Wm^{-2}).

After performing the OLS analysis for clear-sky cases, the analysis was repeated from 3 different cloud fraction bins. We separated clear-sky cases into two separate bins, less than one percent cloud fraction and between one and five percent cloud

fraction, to further reduce cloud contamination. The last bin, between five and fifty percent cloud fraction, represents a portion of the all-sky cases. Pearson's Correlation Coefficient, Spearman's Rank Correlation Coefficient, RMS, MBD, and MAD were calculated for each cloud fraction bin.

One concern is that the five to fifty percent cloud fraction bin has larger samples than the other two bins by an order of magnitude. As a result, we might have misinterpreted the correlations and error statistics from the larger sample size of the five to fifty percent bin. To combat this issue, we used bootstrapping (Efron 1979). Bootstrapping randomly grabbed 500 samples from each bin and calculated Pearson's Correlation Coefficients. This process was repeated 5,000 times to achieve an approximately normal distribution of correlation coefficients. The 95% confidence interval was created from this distribution to determine if the large sample size caused the original correlation coefficient or if it truly represented the data and was not skewed by sample size.

After determining how the outliers vary by cloud fraction bin, we created two time-series to determine if there was any seasonal dependence on the outliers. The observed Mesonet irradiances and measured CERES irradiances were averaged daily for all stations each study year. This was for Terra and Aqua overpass times. The positioning of significant separation between the CERES and Mesonet irradiances gives insight into possible explanations, such as seasonal climate changes, for the cause of the outliers found in the comparison.

The next set of analyses involved looking at the spatial distribution of differences by taking the difference between CERES and Mesonet downward shortwave radiative fluxes (ΔF):

$$\Delta F = F_{\text{CERES}} - F_{\text{Mesonet}} \tag{2.4}$$

where F is the downward shortwave surface irradiance for each instrument. We calculated annual mean irradiance differences for each station after calculating the irradiance differences at the Terra and Aqua overpass times. The stations were placed into the climate divisions defined in Chapter 1 to understand the regional variation of the CERES-Mesonet differences. First, we used box-and-whisker plots to examine CERES-Mesonet differences for all stations and Terra and Aqua overpass times. The lower and upper quartiles represent the 25^{th} and 75^{th} percentiles, respectively. The medians are also displayed with a red center line. The edges of the whiskers (lower and upper extremes) were calculated by using the Turkey Inner Fences method

$$LE = Q_1 - 1.5\,(IQR) \tag{2.5}$$

$$UE = Q_3 + 1.5\,(IQR) \tag{2.6}$$

with LE representing the lower extreme, UE representing the upper extreme, Q_1 representing the lower quartile, Q_3 representing the upper quartile, and IQR representing the interquartile range (Schwertman et al. 2004). The same methodology was used to calculate one box-and-whisker plot for each Terra and Aqua overpass times for each climate division. Like the first box-and-whisker plots, the box-and-whisker plots were averaged over all three years.

In addition, cloud and aerosol properties were analyzed to explore possible sources of the outliers. AOD, cloud fraction, cloud top height, and deep blue single scattering albedo from MODIS radiances were atmospheric variables used to determine if the outliers were primarily caused by cloud or aerosol properties. The annual mean for all variables was plotted for all nine climate divisions. The correspondence of these

aerosol and cloud properties to areas of more prominent outliers will be investigated further to determine if these constituents are a potential explanation for the outliers.

Chapter 3

Results

3.1 Regression of CERES Measured Irradiances on Mesonet Observed Irradiances

3.1.1 Clear-sky Measurements

As mentioned in Section 2.4, the CERES-Terra and CERES-Aqua overpasses were collocated spatially and temporally for each Oklahoma Mesonet station. As the solar zenith angles at 10:30 AM and 1:30 PM are similar in magnitude, the CERES-Terra and CERES-Aqua irradiances should be similar in a clear-sky environment. Recall that a clear-sky environment is defined as having a collocated cloud fraction of 5% or less.

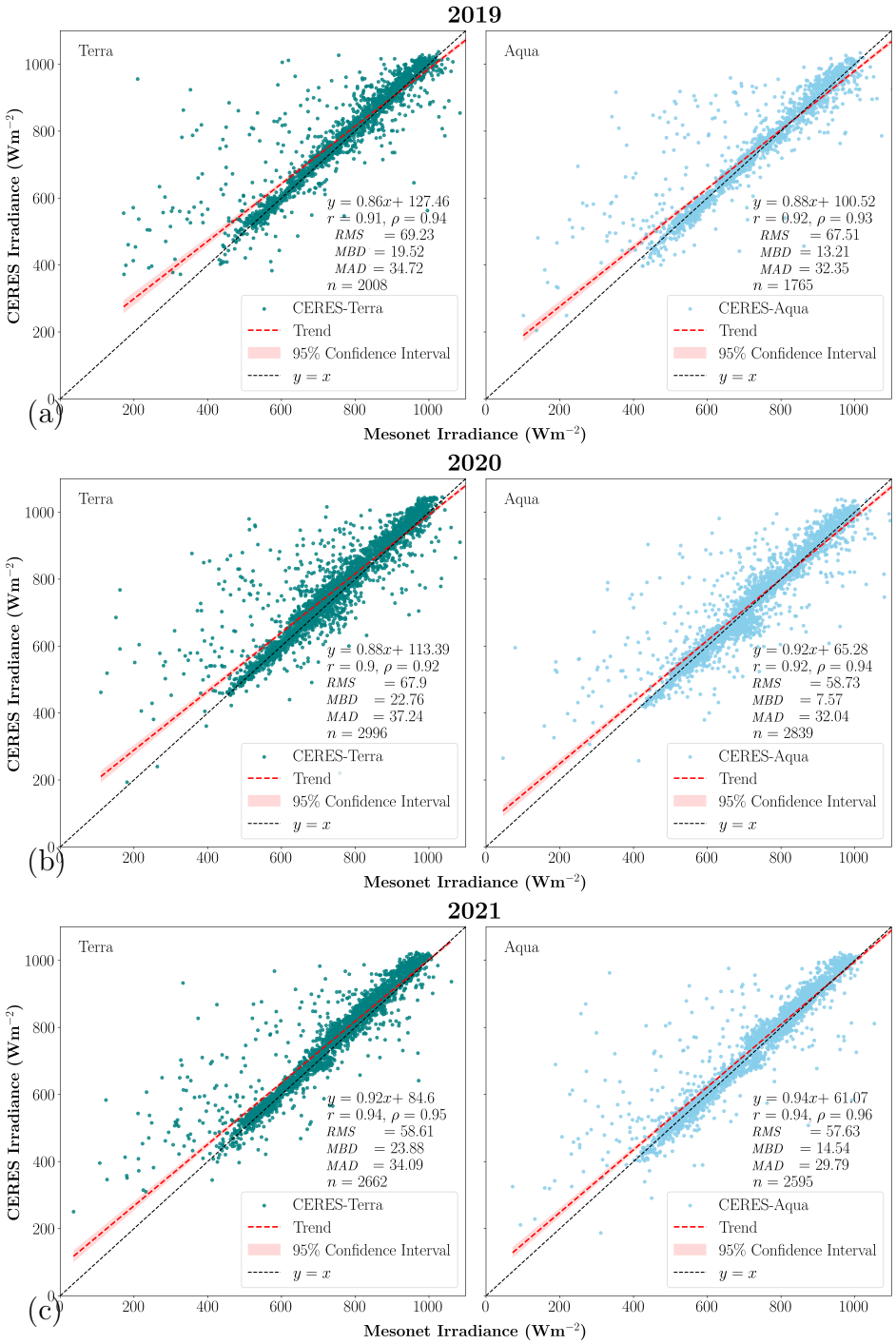

Figure 3.1: CERES Aqua/Terra vs. Mesonet scatterplots at Aqua/Terra overpass times for (a) 2019, (b) 2020, and (c) 2021. Terra points are plotted in green, and Aqua points are in blue. The unity lines are black dashed, and the Ordinary Least Squares linear fit lines are red dashed.

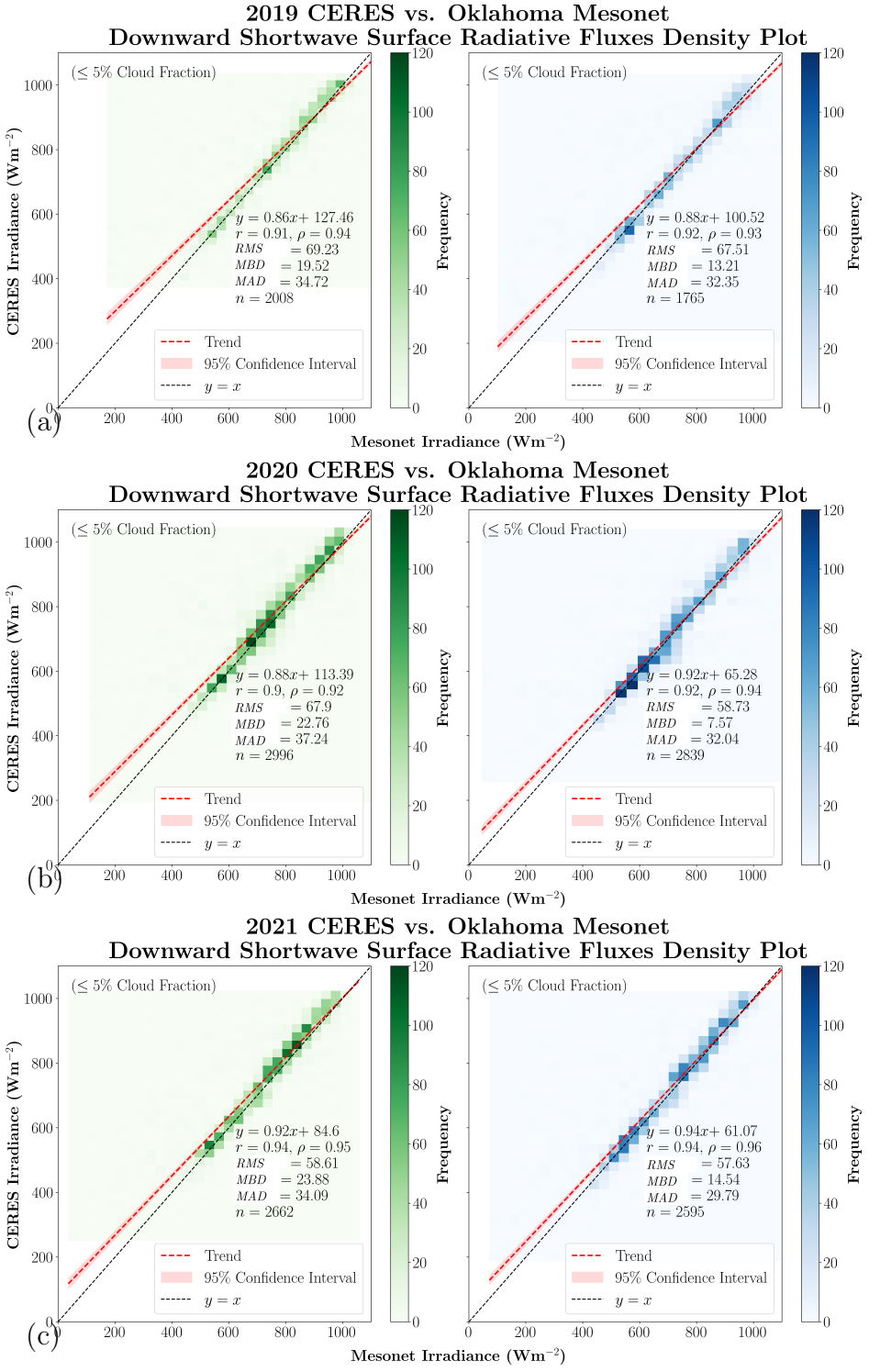

Figure 3.2: CERES vs. Oklahoma Mesonet density-gradient scatterplots for (a) 2019, (b) 2020, and (c) 2021. Terra overpass times are in green, and Aqua are in blue.

The 2019 clear-sky CERES-Terra or CERES-Aqua vs. the Oklahoma Mesonet downward shortwave surface radiative fluxes scatter plot shows all the collocated CERES-Mesonet pairs for the year (Figure 3.1a). As mentioned in Section 2.4, OLS Regression Pearson's Correlation Coefficient, Spearman's Correlation Coefficient, RMS, MBD, and MAD were calculated. The regression coefficients for the Terra and Aqua overpass times are 0.86 and 0.88, respectively. Since the slope is less than one and the offsets are positive, CERES tends to be larger Mesonet, especially at lower irradiances. There also seems to be a clustering above the unity line at large irradiances but at a smaller scale (Figure 3.2a). That said, Pearson's and Spearman's correlation coefficients are larger than 0.9 for Terra and Aqua overpasses, so these outliers represent the minority of cases. For Terra, RMS, MBD, and MAD are 69.23, 19.52, and 34.72 Wm^{-2}. For Aqua, RMS is 67.51, MBD is 13.51, and MAD 32.35 Wm^{-2}. While the difference values aren't very large, Terra overpasses have consistently larger CERES-Mesonet differences than Aqua overpasses. This will be explored later in Section 5.1.

For 2020, the same methodology was used as in the 2019 scatter plots. The regression coefficients were comparable to the 2019 scatter plots (Figure 3.1b). The difference in statistics indicates that the MBD of Terra is 15.19 Wm^{-2} larger than Aqua. RMS and MAD are also larger in magnitude for Terra than Aqua, but not as much as the MBD. The 2D histogram frequency is larger for 2020 than 2019, but that is a function of more cloud-free days in 2020 over 2019 (Figure 3.2b). Other than that, there is robust clustering along the unity line as expected with high correlation coefficient values.

Once again, the same methods were used for the 2021 scatter plots. The correlation coefficients were the largest in 2021, with all values above 0.94 (Figure 3.1c).

The regression coefficients are also larger than 0.9, and the offset is lower for Terra. The MBD is larger for 2021 than for 2020 and 2019. However, the RMS is smaller than in both 2019 and 2020. Therefore, there is less influence from outliers. The 2D histogram shows significant clustering above the unity line, corresponding with approximately 20 Wm^{-2} MBD (Figure 3.2c). Clustering also appears to be closer to the unity line closer to the 600-800 Wm^{-2} range.

3.1.2 All-sky Measurements

Since the clear-sky CERES-Mesonet comparison had relatively high correlation coefficients, the next logical step in the analysis was looking at cases in the presence of clouds. The data was broken up into three cloud fraction bins using the same cloud fraction product as in Section 3.1.1. The three bins are less than one percent cloud fraction, between one and five percent cloud fraction, and between five and fifty percent cloud fraction. These bins were chosen because they represented an even more cloud-free environment and an environment with clouds. The methods for developing the scatter plots are identical to Section 3.3.1.

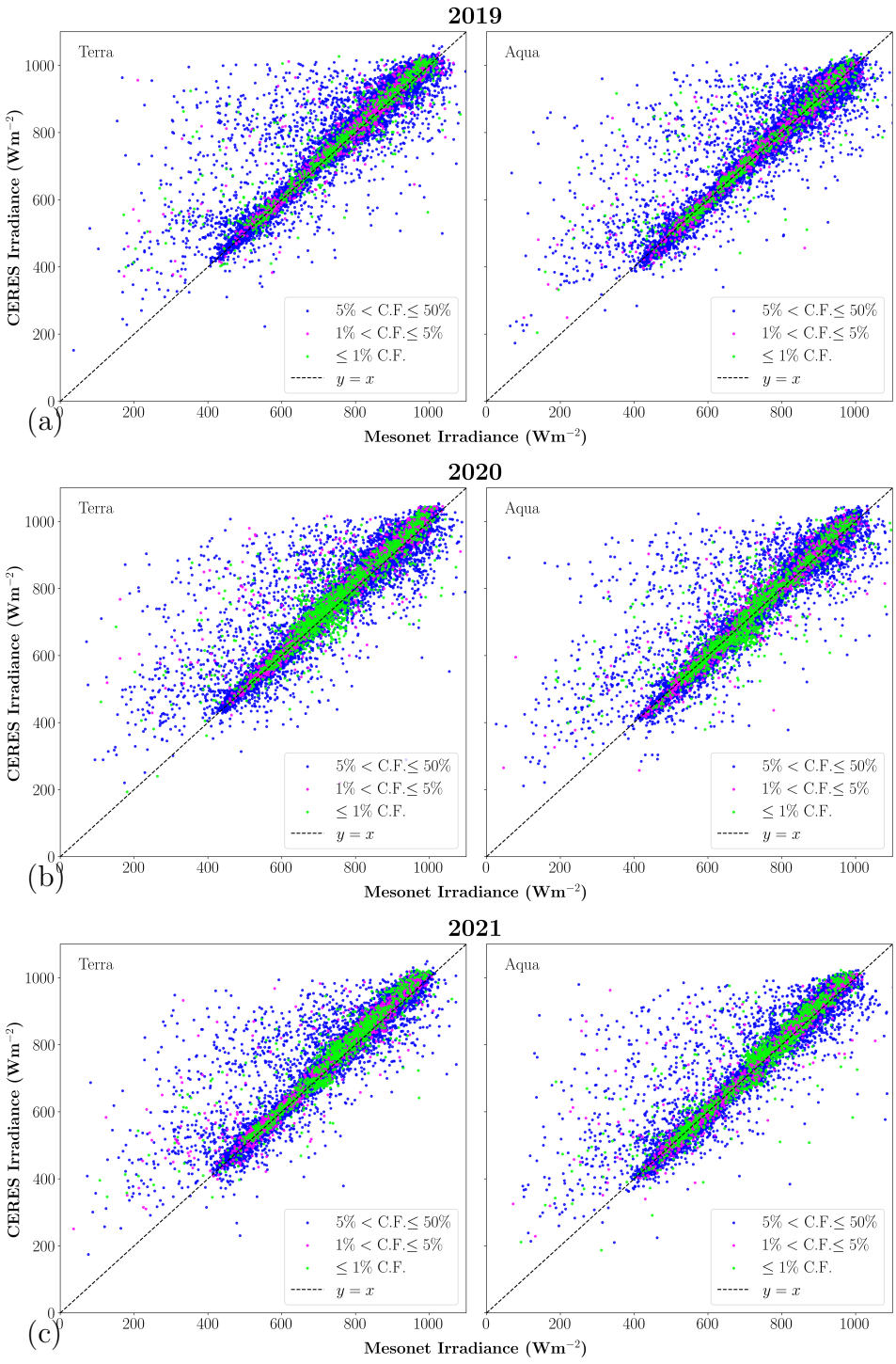

Figure 3.3: CERES Aqua/Terra vs. Mesonet at Aqua/Terra pass times for (a) 2019, (b) 2020, and (c) 2021. The data were separated into three separate bins to determine the performance of the by cloud fraction (Green: 0.00-0.01, Pink: 0.01-0.05, Blue: 0.05-0.50). The unity lines are black dashed.

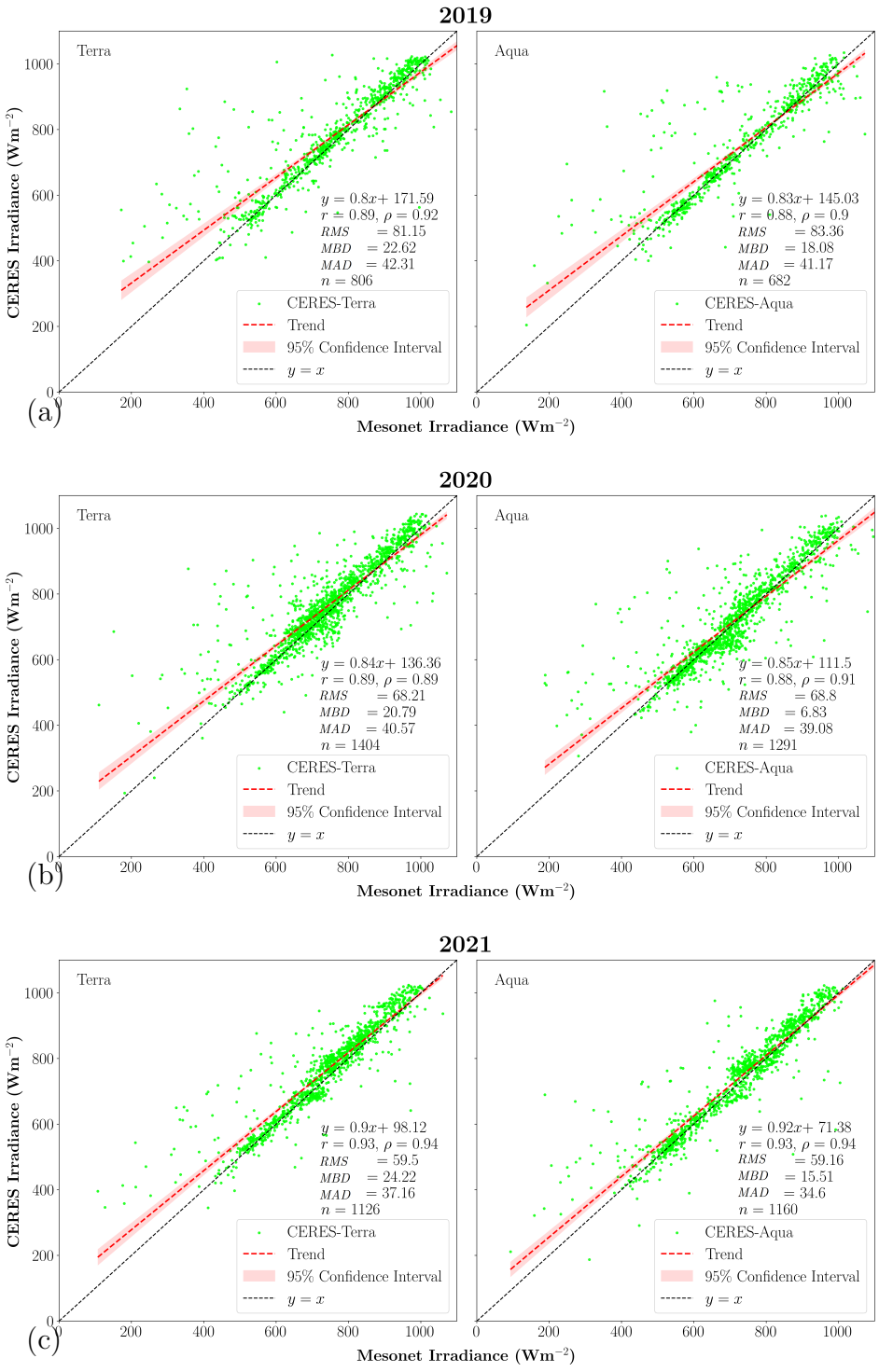

Figure 3.4: Finalized CERES Aqua/Terra vs. Mesonet at Aqua/Terra pass times for (a) 2019, (b) 2020, and (c) 2021. This analysis is for the $\leq 1\%$ cloud fraction bin only. The unity lines are black dashed.

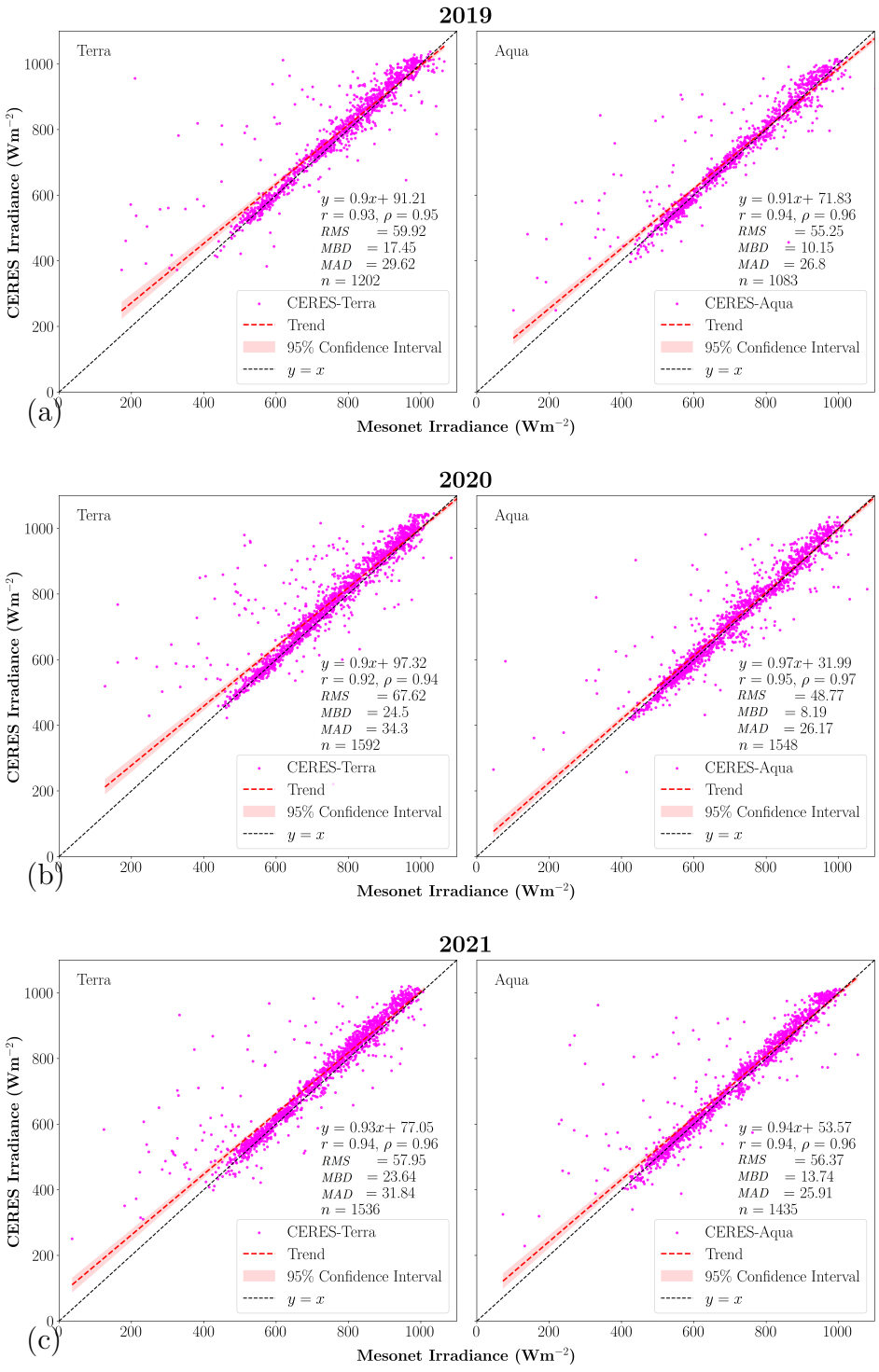

Figure 3.5: CERES Aqua/Terra vs. Mesonet at Aqua/Terra pass times for (a) 2019, (b) 2020, and (c) 2021. This analysis is only for the $1 < \text{C.F.} \leq 5\%$ bin. The unity lines are black dashed.

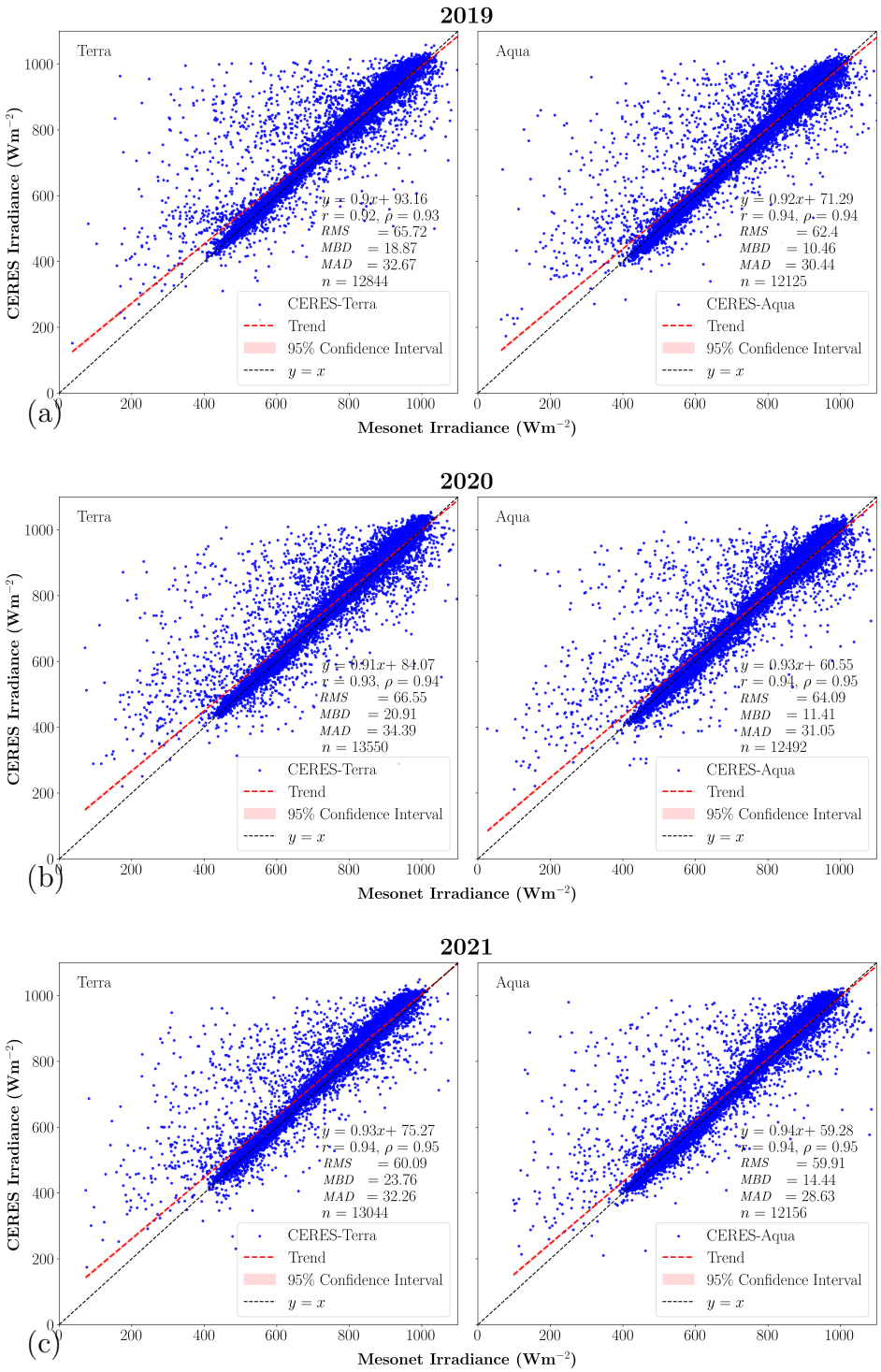

Figure 3.6: CERES Aqua/Terra vs. Mesonet at Aqua/Terra pass times for (a) 2019, (b) 2020, and (c) 2021. This analysis is only for the $5 <$ C.F. $\leq 50\%$ bin. The unity lines are black dashed.

The data for all three cloud fraction bins were plotted on the same figure for 2019, 2020, and 2021 to visually interpret the differences between the three bins (Figure 3.3). At first glance, the highest cloud fraction bin, between five and fifty percent cloud fraction, has the largest number of outliers for all three years. However, since days with higher cloud fractions are much more common in Oklahoma, the higher number of outliers might be just a function of the larger sample size and needs to be evaluated on a relative basis. Qualitatively, 2019 appears to have more outliers than 2020 and 2021, but that will be discussed later from a quantitative perspective.

Table 3.1: Pearson's Correlation (r), Spearman's Correlation (ρ), Root Mean Squared Difference (RMS), Mean Bias Difference (MBD), Mean Absolute Difference (MAD), and number of samples (n) for all three cloud fraction (C.F.) bins for 2019.

Cloud Fraction	**Satellite**	r	ρ	**RMS**	**MBD**	**MAD**	n
C.F. $\leq$ 1%	Terra	0.89	0.92	81.15	22.62	42.31	806
C.F. $\leq$ 1%	Aqua	0.88	0.90	83.36	18.08	41.17	682
1% $<$ C.F. $\leq$ 5%	Terra	0.93	0.95	59.92	17.45	29.62	1202
1% $<$ C.F. $\leq$ 5%	Aqua	0.94	0.96	55.25	10.15	26.80	1083
5% $<$ C.F. $\leq$ 50%	Terra	0.92	0.93	65.72	18.87	32.67	12844
5% $<$ C.F. $\leq$ 50%	Aqua	0.94	0.94	62.40	10.46	30.44	12125

Then, the analysis was separated into individual scatter plots for each cloud fraction bin. Difference statistics were also calculated for each bin (Table 3.1). For 2019 the RMS and MAD are surprisingly much higher than the two other cloud fraction bins (Figures 3.4a, 3.5a, and 3.6a). The MBD is also larger for the smallest cloud fraction bin, which may indicate that large-scale cloud cover is not the dominant driver of uncertainty. Another possibility is that the smaller sample size of the less than one percent cloud fraction bin could mean that outliers are more likely to influence the

difference values. As a result, it is important to look at multiple years of data to see if the pattern holds yearly.

Table 3.2: r, ρ, RMS, MBD, MAD, and n for all three cloud fraction (C.F.) bins for 2020.

Cloud Fraction	**Satellite**	$\boldsymbol{r}$	$\boldsymbol{\rho}$	**RMS**	**MBD**	**MAD**	$\boldsymbol{n}$
C.F. $\leq 1\%$	Terra	0.89	0.89	68.21	20.79	40.57	1404
C.F. $\leq 1\%$	Aqua	0.88	0.91	68.80	6.83	39.08	1291
$1\% <$ C.F. $\leq 5\%$	Terra	0.92	0.94	67.62	24.50	34.30	1592
$1\% <$ C.F. $\leq 5\%$	Aqua	0.95	0.97	48.77	8.19	26.17	1548
$5\% <$ C.F. $\leq 50\%$	Terra	0.93	0.94	66.55	20.91	34.39	13550
$5\% <$ C.F. $\leq 50\%$	Aqua	0.94	0.95	64.09	11.41	31.05	12492

In 2020, the number of clear-sky samples increased (Table 3.2). As a result, we can get a better interpretation of whether or not the small sample size of the 2019 clear-sky results had an impact on why the difference values were higher than the all-sky bin. The correlation coefficients of the less than or equal to one percent cloud fraction bin are still smaller than the other two bins by around 0.03-0.05 (Figures 3.4b, 3.5b, and 3.6b). However, the MBD, RMS, and MAD values are comparable between the three cloud fraction bins with only 3-10 Wm^{-2} difference between the bins on average. Terra's difference values are still larger than Aqua's. In addition, the regression coefficients and y-intercepts are closer to one and smaller, respectively, than the 2019 dataset. As a result, the 2020 comparison features an improved relationship between CERES and Mesonet.

Table 3.3: r, ρ, RMS, MBD, MAD, and n for all three cloud fraction (C.F.) bins for 2021.

Cloud Fraction	**Satellite**	$\boldsymbol{r}$	$\boldsymbol{\rho}$	**RMS**	**MBD**	**MAD**	$\boldsymbol{n}$
C.F. $\leq 1\%$	Terra	0.93	0.94	59.50	24.22	37.16	1126
C.F. $\leq 1\%$	Aqua	0.93	0.94	59.16	15.51	34.60	1160
$1\% <$ C.F. $\leq 5\%$	Terra	0.94	0.96	57.95	23.64	31.84	1536
$1\% <$ C.F. $\leq 5\%$	Aqua	0.94	0.96	56.37	13.74	25.91	1435
$5\% <$ C.F. $\leq 50\%$	Terra	0.94	0.95	60.09	23.76	32.26	13044
$5\% <$ C.F. $\leq 50\%$	Aqua	0.94	0.95	59.91	14.44	28.63	12156

In 2021, the number of clear-sky cases was slightly less than in 2020 but still more than in 2019. The correlation coefficients for all satellites and all cloud fraction bins range from 0.93-0.96. Therefore, there is no appreciable difference in the correlation between the cloud fraction bins. Similarly, there is little change in RMS and MAD by cloud fraction bin. However, MBD for Terra was still approximately 9 Wm^{-2} larger than Aqua's. Therefore, after looking at all the cloud fraction bins and comparing the correlation coefficients and difference values against each other, it appears probable that cloud fraction is not a primary source of difference.

3.1.3 Linear-least Squared Bi-sector Method and Bootstrapping

One downside of OLS regression is that it assumes that the independent variable represents the truth by merit of minimal measurement uncertainty. However, we cannot assume that either variable is true in this study. As a result, we applied the linear-least squared bi-sector method to get a linear regression line more representative of the data. In addition, one concern about calculating Pearson's Correlation

was that the smaller sample size of the clear-sky bins affected its lower correlation coefficient. To get a 95% confidence interval for the correlation coefficients, Monte Carlo bootstrapping was used. The bootstrapping approach randomly selected 500 samples from each bin, then calculated Pearson's correlation for each iteration. Then, the 95% confidence limits on the correlation probability distribution function (PDF) were used for the lower and upper bounds.

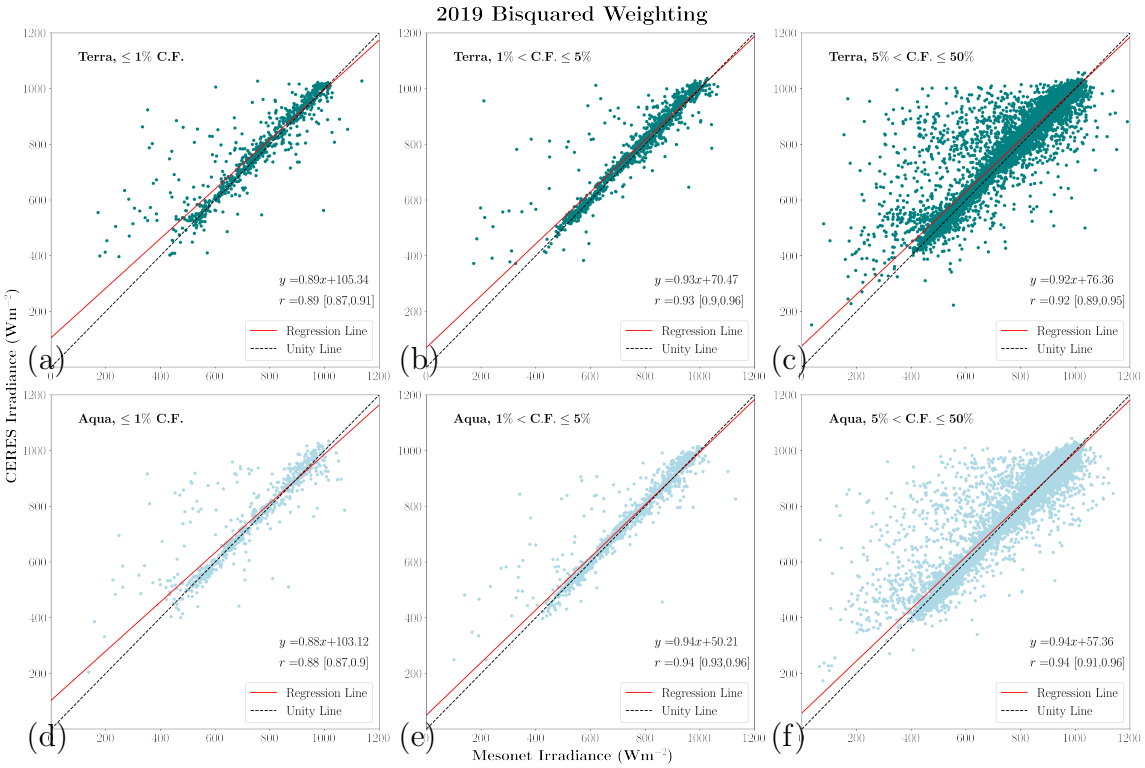

Figure 3.7: Linear-least squared bi-sector fit for CERES Terra/Aqua vs. Mesonet at Terra/Aqua overpass times for (a, d) less than or equal to 1% cloud fraction, (b, e) between 1 and 5% cloud fraction, and (c,f) between 5 and 50% cloud fraction for 2019. r for the bi-sector method is given, with 95% confidence limits in the square brackets.

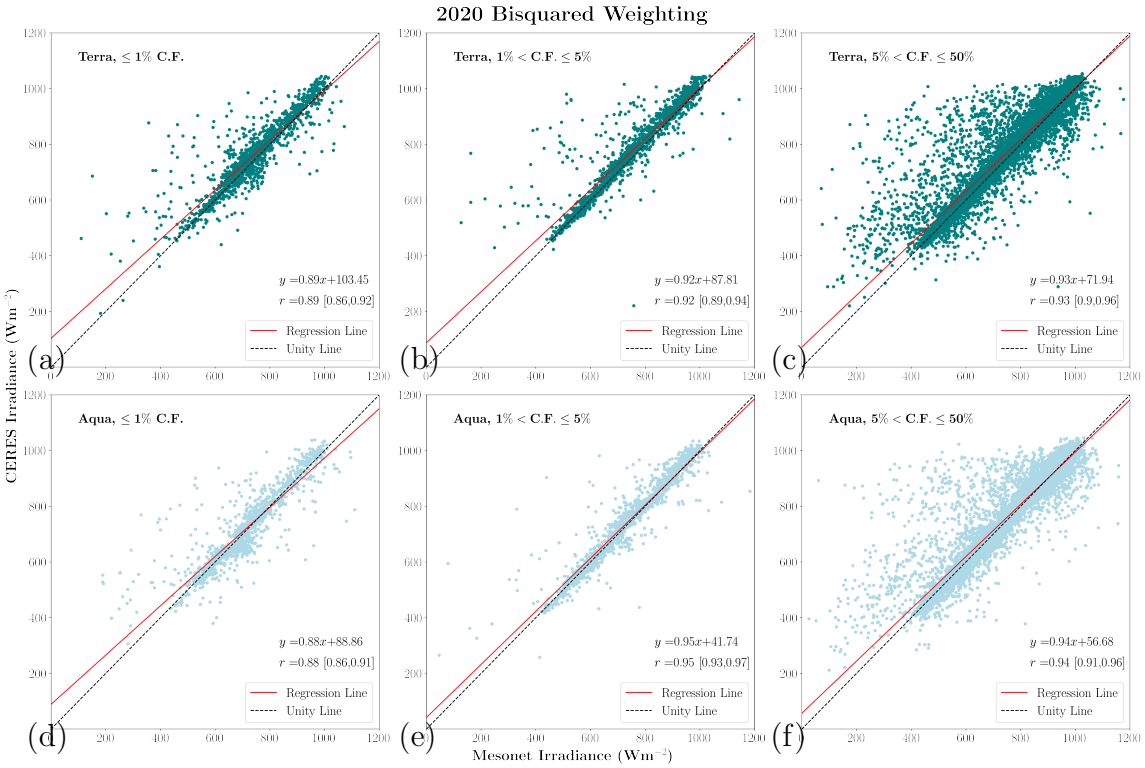

Figure 3.8: Linear-least squared bi-sector fit for CERES Terra/Aqua vs. Mesonet at Terra/Aqua overpass times for (a, d) less than or equal to 1% cloud fraction, (b, e) between 1 and 5% cloud fraction, and (c,f) between 5 and 50% cloud fraction for 2020. r for the bi-sector method is given, with 95% confidence limits in the square brackets.

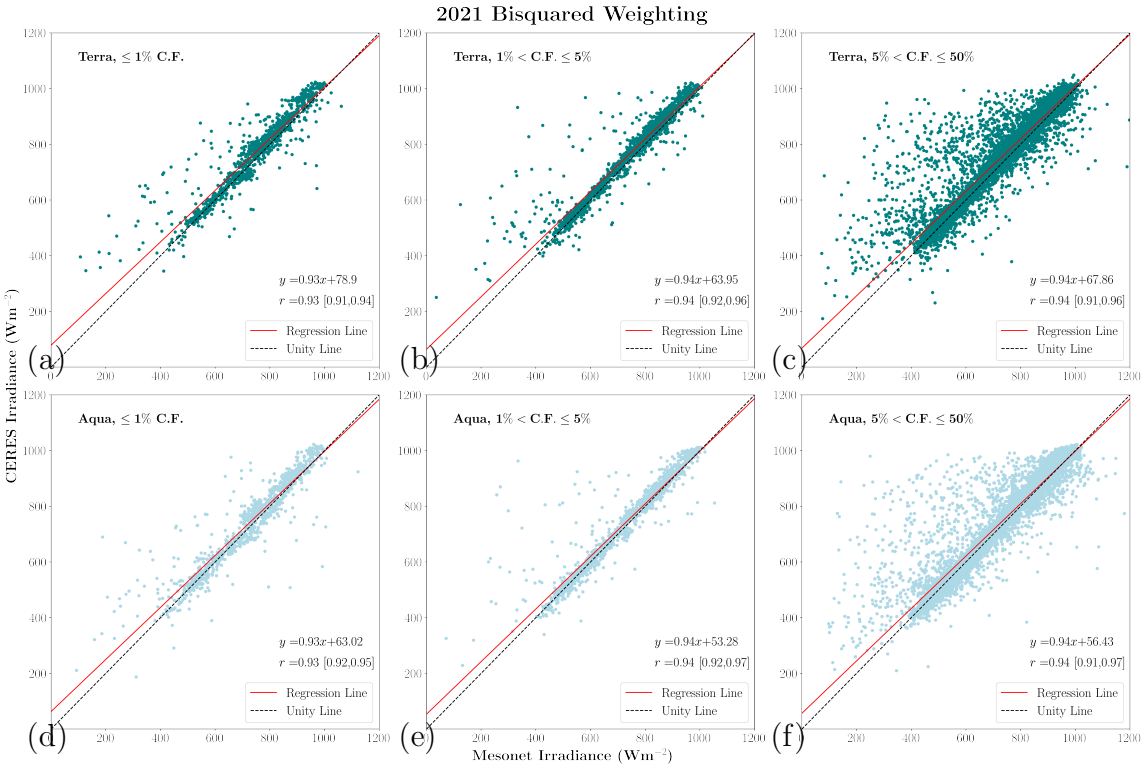

Figure 3.9: Linear-least squared bi-sector fit for CERES Terra/Aqua vs. Mesonet at Terra/Aqua overpass times for (a, d) less than or equal to 1% cloud fraction, (b, e) between 1 and 5% cloud fraction, and (c,f) between 5 and 50% cloud fraction for 2021. r for the bi-sector method is given, with 95% confidence limits in the square brackets.

In 2019, the bi-sector method increased the regression coefficients to match Pearson's correlation coefficients for all three cloud fraction bins for both Aqua and Terra (Figure 3.7). This occurred for both the 2020 and 2021 data. This means the regression lines represent the organization of the CERES-Mesonet differences (Figures 3.8 and 3.9). While the outliers slightly influence the bi-sector method, it is much more representative of the actual pattern. The 95% confidence interval from the bootstrapping is found in the brackets next to the correlation coefficients. All of Pearson's Correlations lie within the confidence interval, which means we can say that the correlations were not influenced by sample size. Therefore, the bi-sector method is the primary regression used in the discussion.

3.2 Time-series Analysis

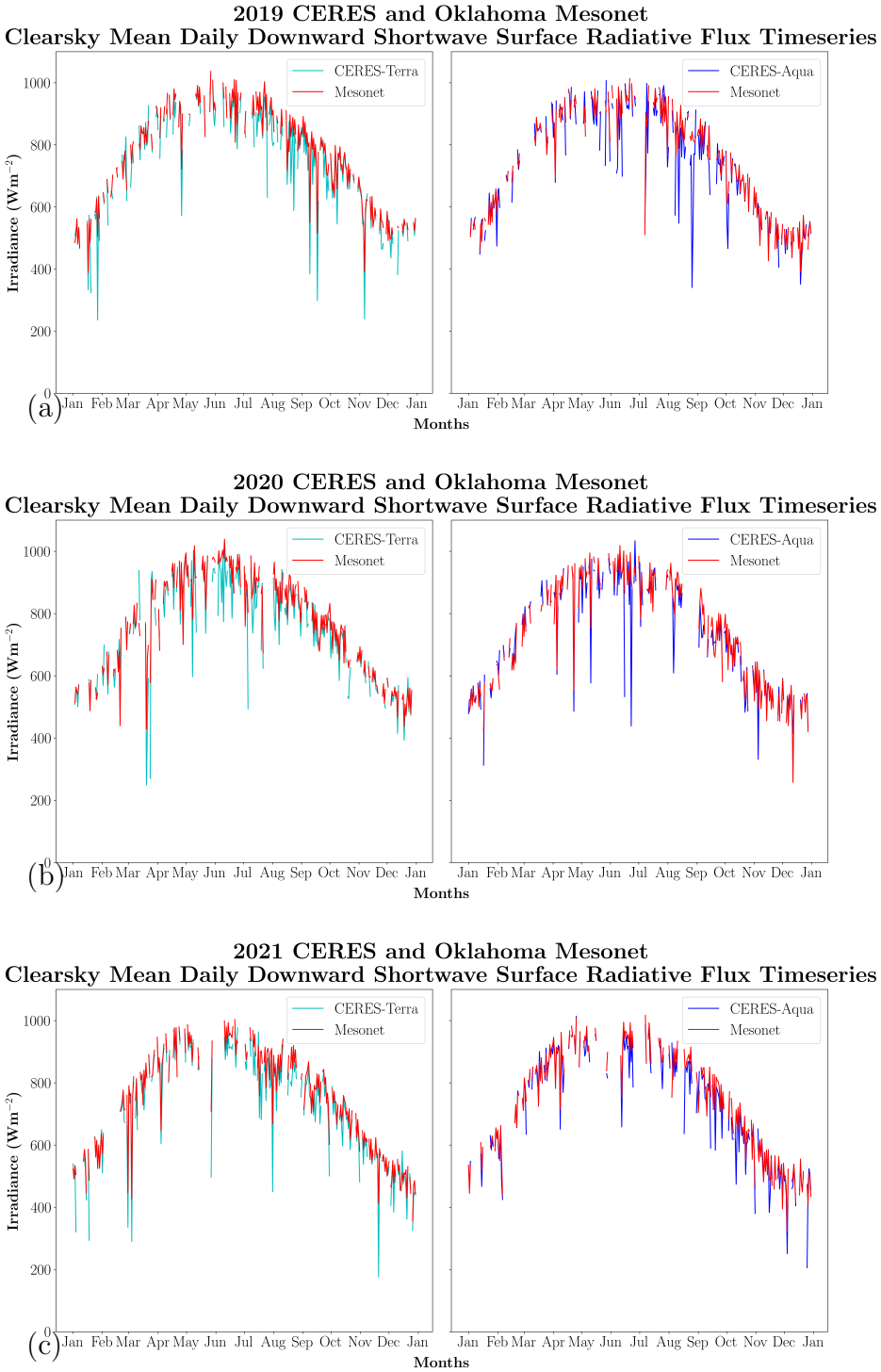

Figure 3.10: Clear-sky Surface downwelling shortwave fluxes for CERES (Terra in teal, Aqua in blue) and Mesonet Timeseries (in red) for (a) 2019, (b) 2020, and (c) 2021.

Figure 3.10 shows the seasonal evolution of Mesonet and CERES irradiances for clear-sky conditions. The peak difference between CERES-Aqua and Mesonet in 2019 and 2020 occurs during the convective season, May through September. There appears to be less of a CERES-Mesonet difference in late Summer 2021. Outside the convective season, there is much more alignment between CERES and Mesonet. CERES-Terra has a higher separation from Mesonet during this period than Aqua. This is verified by the higher year-to-year MBD values in Terra for all three years (Tables 3.1, 3.2, and 3.3).

3.3 Geospatial Analysis

One of the benefits of performing the study in Oklahoma is the presence of diverse climate zones, topography, and landscapes. These characteristics enable the results of this study to be applied all over the globe for similar climates. The geospatial analysis was conducted to understand the differences and uncertainty associated with each climate regime.

3.3.1 CERES-Mesonet Differences Statistics

We calculated the Mesonet-CERES downwelling shortwave irradiance differences for each station using Eq. 2.5. Then, the annual means and standard deviations were calculated for each Mesonet station. The irradiance differences were calculated for all cloud fractions. Then, they were examined to determine if there were any consistent patterns regionally each year.

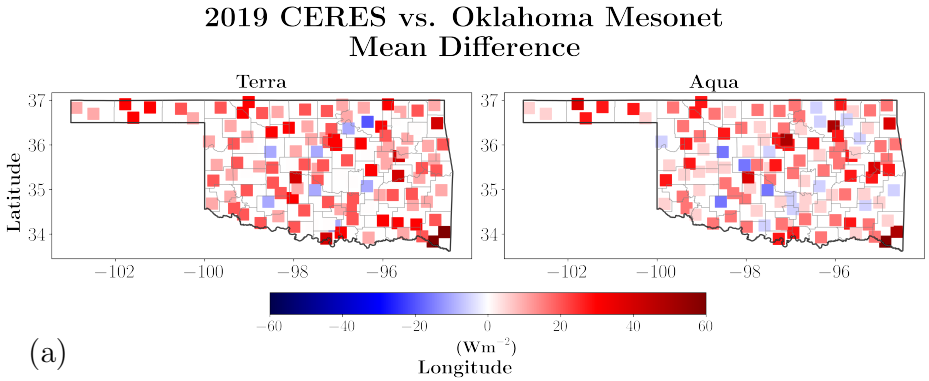

(a)

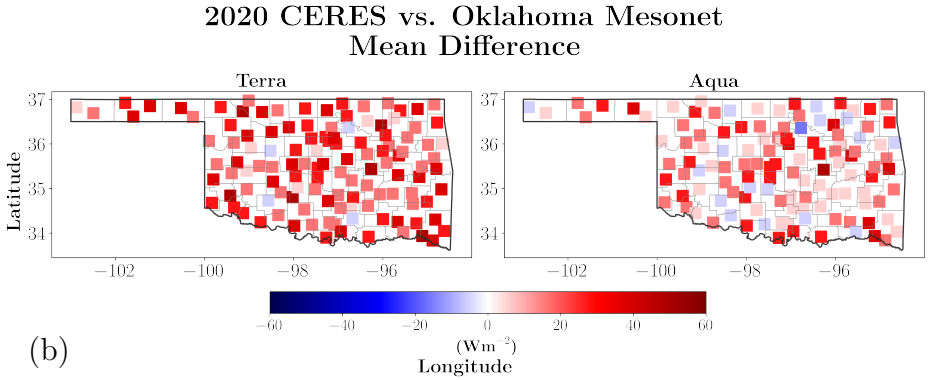

(b)

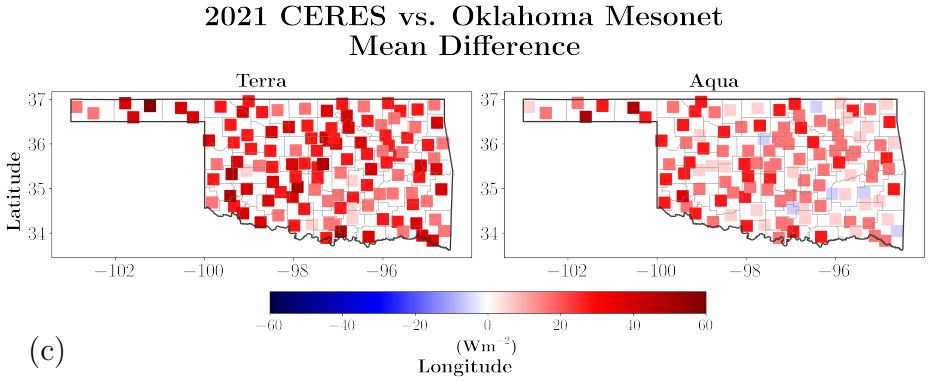

(c)

Figure 3.11: The mean flux differences of Mesonet from CERES in (a) 2019, (b) 2020, and (c) 2021 with red squares indicating CERES was larger than Mesonet and blue squares showing lower CERES irradiances than Mesonet.

In 2019, the mean difference between CERES and Mesonet was highest in the southeast climate zone. CERES exceeded Mesonet at the Idabel and Broken Bow stations by approximately 60 Wm^{-2} on average (Figure 3.11a). Additionally, the Stillwater area had large CERES-Mesonet differences on the order of 20-50 Wm^{-2}. Also, the central panhandle stations, Eva, Goodwell, and Hooker, had CERES-Mesonet differences around 30 Wm^{-2}. Consistent with the scatter plots in Section 3.1, Terra had larger CERES-Mesonet differences than Aqua. There are 7 out of the 120 stations where CERES-Terra mean differences are less than Mesonet.

In 2020, CERES-Terra had even fewer measurements where the mean downward shortwave surface radiative flux difference was smaller than the Mesonet stations (Figure 3.11b). Only 4 out of 120 stations had this characteristic, and all four had values larger than CERES in 2019. In addition, CERES-Terra and CERES-Aqua are larger than Mesonet in the central panhandle. The Stillwater area stations still show large CERES-Mesonet differences, but not as large a magnitude as in 2019. The Idabel and Broken Bow areas still had large CERES-Mesonet difference during Terra overpasses, but Aqua only had CERES-Mesonet differences of approximately 5 Wm^{-2} at these stations.

Finally, in 2021, Terra had positive CERES-Mesonet differences for all 120 stations (Figure 3.11c). There seemed to be no spatial pattern with the CERES-Mesonet differences in 2021, and it was systematic across all 120 stations. The central panhandle continued to show large CERES-Mesonet differences for the CERES-Aqua data. Interestingly, the Idabel and Broken Bow Mesonet stations report similar irradiances to CERES-Terra/Aqua, unlike in 2019 and 2020 (for Terra).

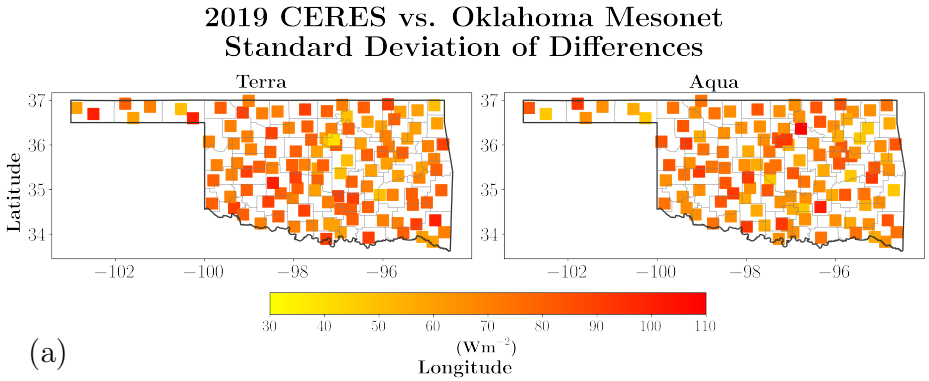

(a)

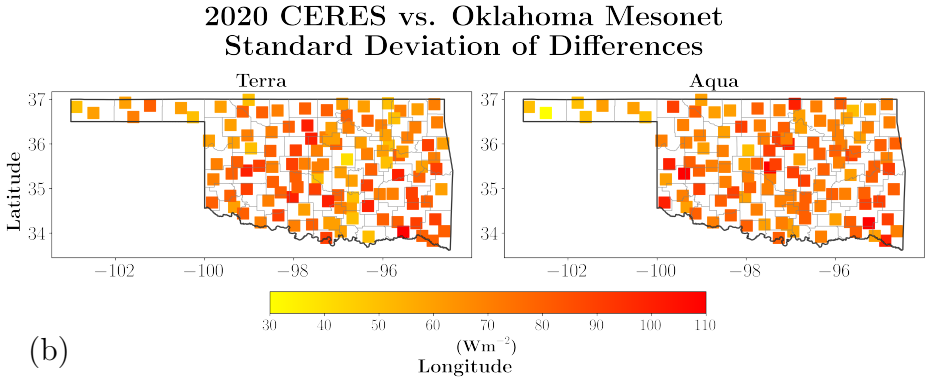

(b)

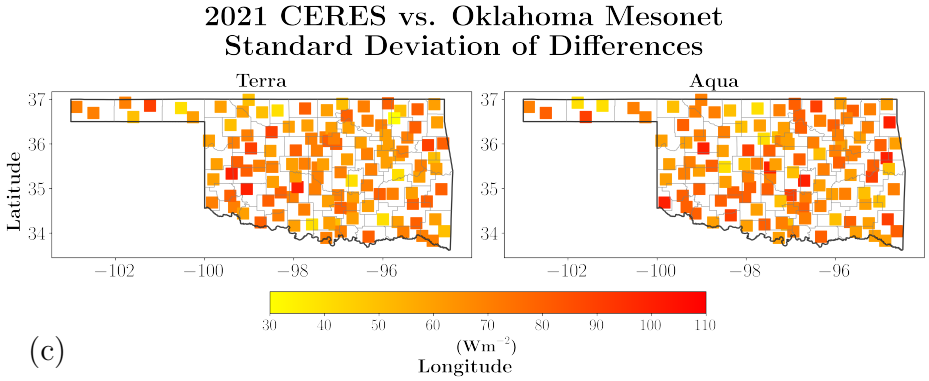

(c)

Figure 3.12: The standard deviations of the differences of Mesonet from CERES in (a) 2019, (b) 2020, and (c) 2021 with yellow and red squares representing smaller and larger magnitudes of standard deviation, respectively.

While the mean difference plots give a general interpretation of which stations tend to have higher differences, they do not show the data distribution. The mean standard deviation of the flux differences shows which stations are more influenced by outliers.

In 2019, there was a slight variation in the standard deviation by region (Figure 3.12a). There was also little difference in the standard deviations between Terra and Aqua. In 2020, two distinct regions with higher standard deviations stood out: the southeast and the western regions, excluding the panhandle (Figure 3.12b). The panhandle tends to have lower standard deviations than the rest of the state. The rest of the standard derivations had no consistent pattern in 2020. There were little variations in the spatial pattern between Terra and Aqua in 2020. In 2021, the western regions, excluding the panhandle and the southeast regions still has the highest standard deviations (Figure 3.12c). With a few exceptions, the panhandle still has lower standard deviations than the other regions. Unlike 2019 and 2020, Aqua did have, on average, lower standard deviations of differences than Terra in 2021.

3.3.2 Distribution of Outliers

While the standard deviation of the differences plots provided an idea of the overall distribution of the CERES-Mesonet differences, it is not an accurate count of all the outliers by region. In addition, the analysis was done annually and not combined for all three years. The data were standardized using a normal distribution to determine which areas of Oklahoma have the most outliers. The z-scores are the mean CERES-Mesonet difference subtracted from each difference divided by the standard deviation. These were calculated for each CERES-Mesonet difference.

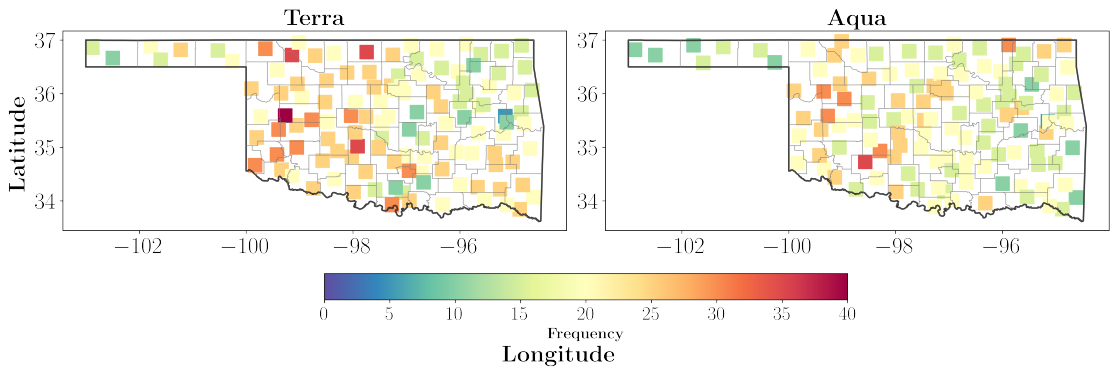

Figure 3.13: The frequency of observations with a CERES-Mesonet difference greater than 1.96 standard deviations away from the mean per Mesonet station.

After calculating the z-scores, the number of times the CERES-Mesonet difference exceeded the 95% confidence interval, and the z-score was greater than or equal to 1.96 was determined per station. The distribution of these differences was plotted (Figure 3.13). The western half of Oklahoma, excluding the panhandle, had the most outliers for Terra and Aqua overpass times. The panhandle had the lowest points that exceeded 1.96 standard deviations away from the mean for both Terra and Aqua. For Terra overpasses, the northeast climate division had few, approximately 15, measurements that exceeded the 95% confidence interval. In contrast, during the Aqua overpasses, the count nearly doubled with approximately 30 measurements per station, where the difference calculations exceeded 1.96 standard deviations away from the mean. The southeast climate division had a larger number of high z-scores for the Terra overpass times than the Aqua overpass times, which was analogous to the general pattern with Terra having higher MBD than Aqua.

3.4 Climate Division Analysis

The previous section provided an overview of which regions have the most outliers. However, it did not indicate each climate zone's overall PDF. The best way to determine how the distribution of the CERES-Mesonet differences changes with climate zone is to make box-and-whisker plots.

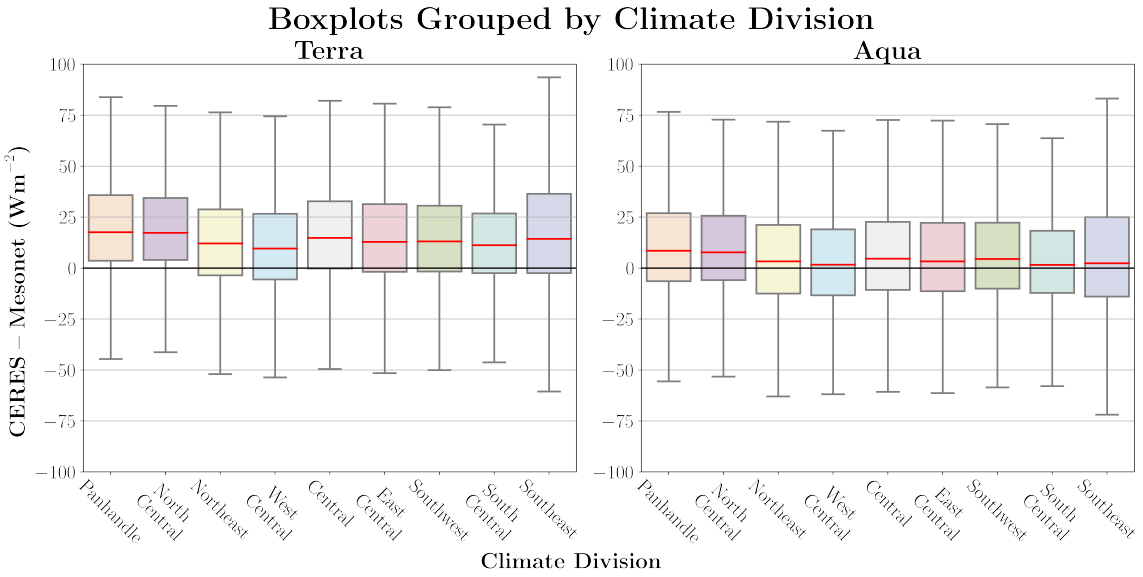

Figure 3.14: All-sky CERES-Mesonet surface downwelling irradiances differences box-and-whisker plots by climate division for 2019-2021. Red lines are the median of each division, and the colors of each box match the colors of the climate divisions shown in Figure 2.1.

Figure 3.14 shows box-and-whisker plots created for all-sky irradiances. The lower quartile for the panhandle and north central regions during the Terra overpass time is above zero, indicating that CERES Terra irradiances are larger than Mesonet irradiances over 75% of the time. The range and interquartile range are much larger in the southeast region. Greater Mesonet station density in the central region might be a reason for the lower standard deviation. That said, the station density in the

southeast region is larger than the panhandle and has a larger standard deviation. Therefore, it is likely that some systematic differences in the panhandle are causing the large range and interquartile range.

3.5 Seasonal Dependence

3.5.1 Flux Differences Distributions

The cloud and aerosol properties vary seasonally in addition to regionally. As a result, it is important to look at both the PDFs of the climate zone and seasonal CERES-Mesonet surface irradiance differences. The seasonal box-and-whisker plots are for all-sky and clear-sky environments to determine which differences are most likely cloud or aerosol driven.

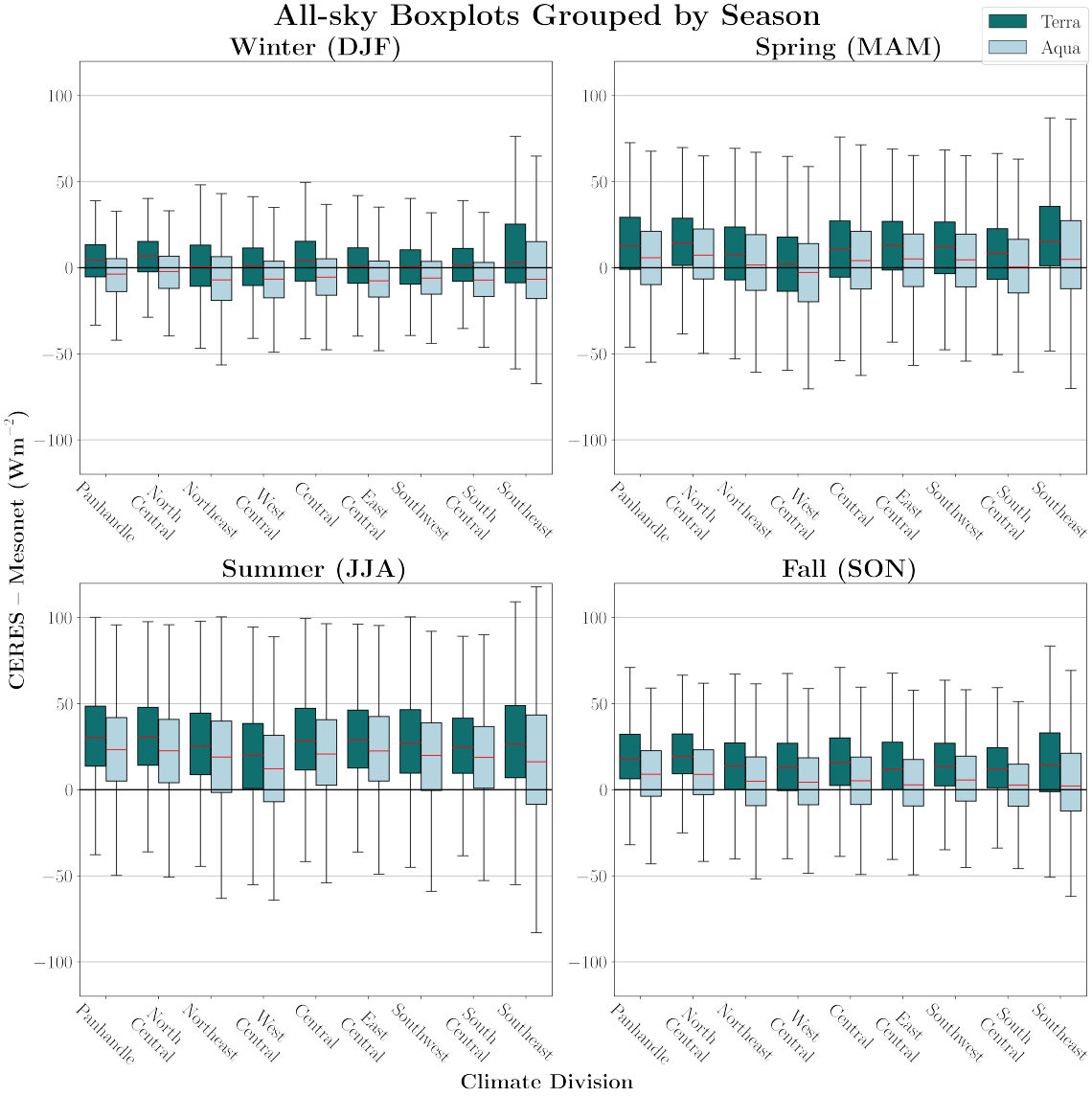

Figure 3.15: All-sky CERES-Mesonet surface downwelling irradiances differences box-and-whisker plots by climate division and season for 2019-2021. Red lines are the median irradiance difference for each division, green boxes are for Terra overpass times, and blue boxes are for Aqua overpass times.

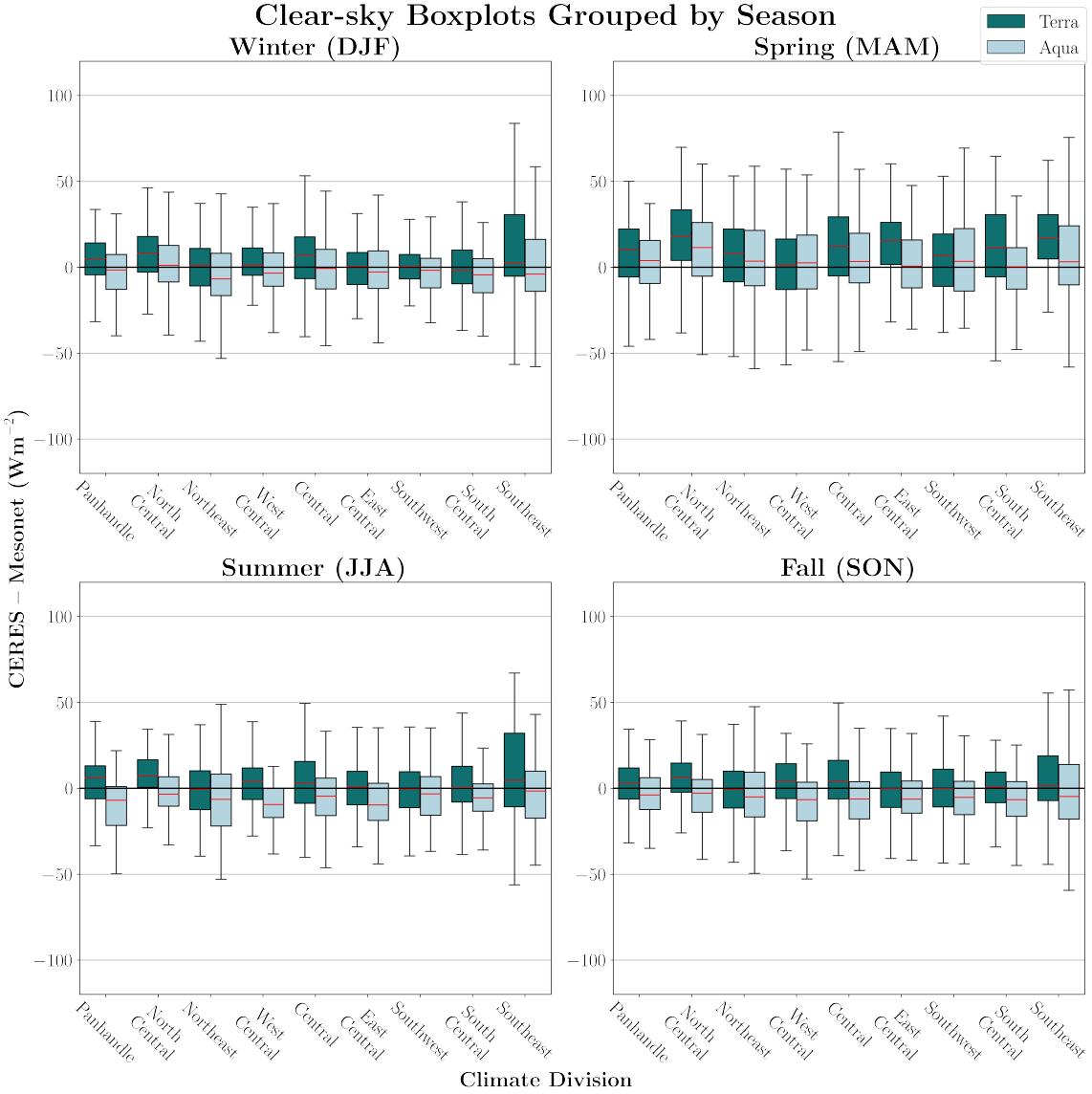

Figure 3.16: Clear-sky CERES-Mesonet surface downwelling irradiances differences box-and-whisker plots by climate division and season for 2019-2021. Red lines are the median irradiance difference for each division, green boxes are for Terra overpass times, and blue boxes are for Aqua overpass times.

The box-and-whisker plots showed distinct seasonal patterns for the all-sky conditions (Figure 3.15). In the northern hemispheric winter, the ranges and interquartile ranges for all nine climate zones were the lowest of all the seasons. The medians for both Terra and Aqua are very close to zero CERES-Mesonet difference. Interestingly, the Terra overpass medians are greater than zero for all nine climate divisions, and the Aqua overpass medians are less than zero. The southeast climate zone has a much larger standard deviation than the other climate divisions in the winter.

In the spring, the standard deviation increases in all the climate zones except for the southeast region. The southeast region still has the largest standard deviation, but range and interquartile roughly remain the same as winter cases. The other major change from the spring is that Terra and Aqua now have medians over zero for eight out of nine climate divisions. Terra still has a larger CERES-Mesonet median difference for all nine climate zones.

In the summer, the standard deviation is considerable for all nine climate zones. The medians for all nine climate zones are now significantly above zero. Terra differences are still larger than Aqua for all the climate zones, and the median difference of differences from Mesonet to Terra and Aqua CERES, respectively, is 5 Wm^{-2}. The southeast region still has the largest standard deviation out of all the climate zones.

The fall box-and-whisker plots look almost identical to the spring plots. There is little variation in the ranges and interquartile ranges of the climate zones, except for the southeast region. The Terra and Aqua medians appear slightly larger than the spring medians. Terra still has larger medians than Aqua for all climate zones, and both Terra and Aqua overpasses are above zero.

The clear-sky results are very different from the all-sky results (Figure 3.16). The major difference is less seasonal dependence with the clear-sky results than with all-sky results. The spring clear-sky plots have the highest ranges and interquartile ranges of the four seasons. Summer, fall, and winter have roughly the same ranges and interquartile ranges as a whole. Another interesting component of the comparisons is that the median Aqua differences are negative for winter, summer, and fall. Furthermore, the southeast region still has the highest range and interquartile range for the winter, summer, and fall.

3.5.2 Seasonal Scatterplots

While examining the box-and-whisker plots by season gives a general idea of the temporal distribution of the CERES-Mesonet difference, they do not show the individual data points. Visualizing the individual points for all-sky and clear-sky environments is important for justifying the hypothesis examined in the previous section. The best-fit line was calculated using the bi-sector method, and the confidence intervals for Pearson's correlations were done using bootstrapping.

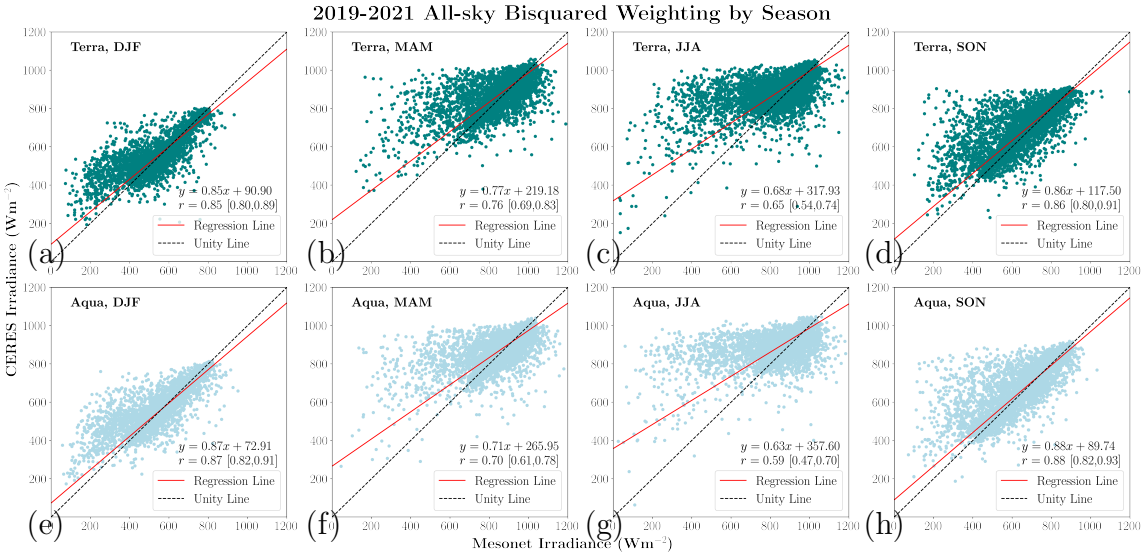

Figure 3.17: Linear-least squared bi-sector fit for all-sky CERES Aqua/Terra vs. Mesonet for (a, e) winter, (b, f) spring, (c, g) summer, and (d, h) fall in 2019-2021. r for the seasonal bi-sector regression and bootstrapped 95% confidence interval are given.

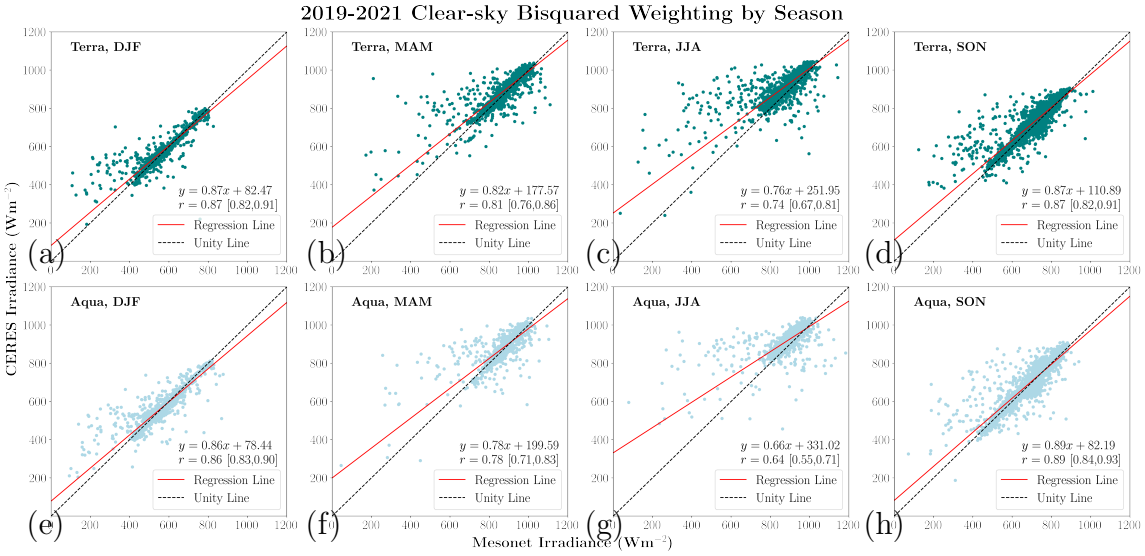

Figure 3.18: Linear-least squared bi-sector fit for clear-sky CERES Aqua/Terra vs. Mesonet for (a, e) winter, (b, f) spring, (c, g) summer, and (d, h) fall in 2019-2021. r for the seasonal bi-sector regression and bootstrapped 95% confidence interval are given.

The seasonal all-sky comparisons show a stark contrast between seasons for both Terra and Aqua overpasses (Figure 3.17). In the northern hemispheric winter, the correlation between CERES and Mesonet is relatively strong, with Pearson's correlation values of 0.85 and 0.87 for Terra and Aqua, respectively. Unlike the winter scatterplots, the spring and summer plots have much lower correlations.

Finally, the fall scatter plots resemble the winter scatterplots with strong positive correlation coefficients. The regression coefficients match the correlation coefficients indicating that the line of best fits matches the trends. In addition, all correlations for all seasons lie in the 95% confidence interval indicating that the correlations should be similar with a smaller sample size.

The clear-sky results do have some differences from the all-sky results. Like the previous figures, a clear-sky atmosphere was defined by eliminating cases with a collocated cloud fraction greater than five percent. The winter and fall clear-sky scatterplots are similar to the all-sky scatterplots (Figure 3.18). However, there were major differences between the clear-sky and all-sky springs and summers for both Terra and Aqua. There was a 0.09 increase in the correlation coefficient for Terra and a 0.05 increase for Aqua overpasses in the clear-sky scatterplots. In addition, the summer correlation coefficient for Aqua is much lower than Terra. All correlations are within the bootstrapped 95% confidence interval, indicating the sample size does not explain the higher or lower correlation coefficients.

Table 3.4: r, ρ, RMS, MBD, MAD, and n by season in 2019-2021.

Season	**Atmo-sphere**	**Satellite**	$\boldsymbol{r}$	$\boldsymbol{\rho}$	**RMS**	**MBD**	**MAD**	$\boldsymbol{n}$
Winter	All-sky	Terra	0.85	0.87	53.18	8.95	26.09	11379
Winter	All-sky	Aqua	0.87	0.89	52.44	1.36	26.30	12039
Winter	Clear-sky	Terra	0.87	0.91	51.26	8.91	23.88	1221
Winter	Clear-sky	Aqua	0.86	0.88	50.77	3.66	25.55	1485
Spring	All-sky	Terra	0.76	0.84	73.74	17.70	37.57	12053
Spring	All-sky	Aqua	0.70	0.82	75.52	11.67	36.90	11578
Spring	Clear-sky	Terra	0.81	0.88	69.43	17.16	36.07	1316
Spring	Clear-sky	Aqua	0.78	0.86	64.77	9.31	21.91	1229
Summer	All-sky	Terra	0.65	0.77	91.34	38.15	51.91	15078
Summer	All-sky	Aqua	0.59	0.71	95.89	31.23	50.57	12193
Summer	Clear-sky	Terra	0.74	0.83	87.07	41.01	51.68	1838
Summer	Clear-sky	Aqua	0.64	0.76	91.83	32.27	51.17	1136
Fall	All-sky	Terra	0.86	0.91	61.79	21.69	32.35	18637
Fall	All-sky	Aqua	0.88	0,92	57.70	11.55	28.06	17698
Fall	Clear-sky	Terra	0.87	0.91	52.57	18.88	30.51	3291
Fall	Clear-sky	Aqua	0.89	0.92	48.55	8.66	26.90	3349

For both the all-sky and clear-sky cases, the same difference statistics calculated for the yearly scatterplots were calculated with the seasonal scatterplots (Table 3.4). In addition to the correlation coefficients being smaller during the summer, the difference values were much larger. The RMS for clear-sky and all-sky environments averaged about 91 Wm^{-2}. The summer MBD was also much larger than the other seasons, with a mean value of 33.16 Wm^{-2}. That is just under 20 Wm^{-2} larger than the spring and fall, and just under 30 Wm^{-2} larger than the winter. While difference

values are generally higher for Terra than Aqua, that trend changes in the summertime. The RMS is about 4 Wm^{-2} larger for Aqua than Terra for clear-sky and all-sky contamination, even though the MBD is larger in the Terra overpasses. Consistent with the correlation coefficients, the spring has the second largest RMS, and the Fall and Winter have the lowest RMS. Overall, all seasons, except the summer, have a relatively low difference, and the simple parameterized code does a phenomenal job at resolving the downward shortwave irradiances from the TOA.

3.5.3 Robust Outlier Rejection

Even though we applied cloud fraction to indicate clear-sky environments, the results suggest it is not an excellent filter to eliminate small cloud obstruction. We observed little change in correlation with an increase in cloud fraction every year. This section describes the results of applying a robust outlier rejection to remove potentially small-cloud affected observations. This function eliminated samples outside three standard deviations from the mean.

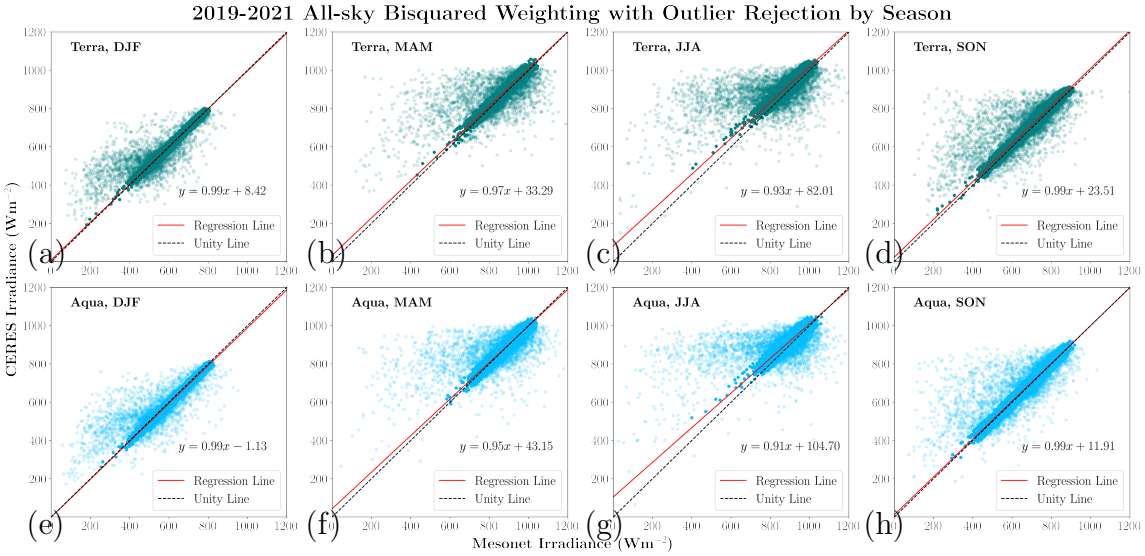

Figure 3.19: Linear-least squared bi-sector fit with outlier rejection all-sky CERES Aqua/Terra vs. Mesonet for (a, e) winter, (b, f) spring, (c, g) summer, and (d, h) fall in 2019-2021.

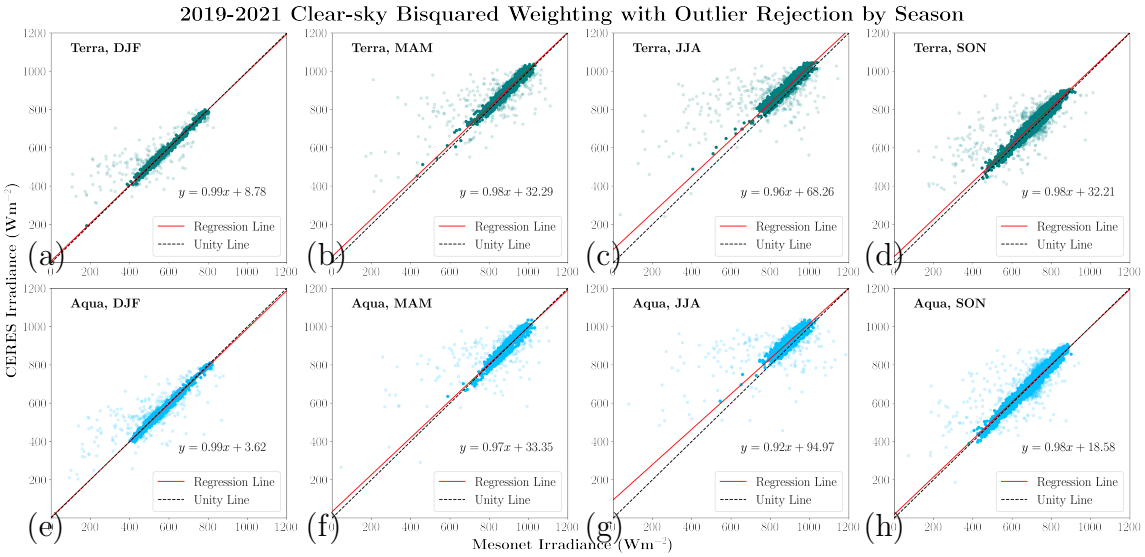

Figure 3.20: Linear-least squared bi-sector fit with outlier rejection clear-sky CERES Aqua/Terra vs. Mesonet for (a, e) winter, (b, f) spring, (c, g) summer, and (d, h) fall in 2019-2021.

Table 3.5: RMS, MBD, MAD, and n by season in 2019-2021 with outlier rejection.

Season	**Atmosphere**	**Satellite**	**RMS**	**MBD**	**MAD**	$\boldsymbol{n}$
Winter	All-sky	Terra	12.30	1.77	10.00	9275
Winter	All-sky	Aqua	14.13	−6.71	11.36	9899
Winter	Clear-sky	Terra	12.51	2.06	10.05	1025
Winter	Clear-sky	Aqua	13.12	−3.74	10.53	1198
Spring	All-sky	Terra	20.75	10.35	16.82	9892
Spring	All-sky	Aqua	19.69	2.94	15.67	9592
Spring	Clear-Sky	Terra	20.42	10.78	16.69	1068
Spring	Clear-sky	Aqua	10.13	2.79	14.45	1041
Summer	All-sky	Terra	33.11	26.24	28.16	12281
Summer	All-sky	Aqua	29.56	18.88	24.30	10017
Summer	Clear-sky	Terra	36.32	30.44	31.43	1537
Summer	Clear-sky	Aqua	32.81	24.96	27.53	945
Fall	All-sky	Terra	21.75	14.55	17.81	15942
Fall	All-sky	Aqua	17.39	4.57	13.96	15170
Fall	Clear-sky	Terra	24.32	14.86	19.79	2915
Fall	Clear-sky	Aqua	20.44	5.48	16.34	2947

After restricting to clear-sky cases, we calculated new regression coefficients and intercepts (Figures 3.19 and 3.20). The new regression coefficients for the winter and fall were both 0.99 for all-sky conditions. While the winter regression coefficients remained at 0.99 for clear-sky, there was a slight decrease in the regression coefficients in the fall to 0.98. This indicates that there are minimal CERES-Mesonet differences in the winter and fall.

Before the robust outlier rejection, regression coefficients for the summer were 0.66 for Aqua and 0.76 for Terra for clear-sky, and 0.59 and 0.65 for Aqua and Terra,

respectively, for all-sky. Also, all difference values were reduced for robust outlier versus unfiltered cases. The average RMS for the winter, spring, and fall is 16.41 Wm^{-2}, while the summer averaged RMS for all instances is 32.95 Wm^{-2}. That means the summer still has 100% larger differences than the average of the other three months. The MBD and MAD, while reduced versus the unfiltered cases, are still much larger in the summer. This could still be partly due to cloud contamination, but absorbing aerosol contamination could contribute to the larger differences.

Chapter 4

Discussion

4.1 Potential Sources of Error

4.1.1 Terra vs. Aqua

One finding was the systematically larger CERES-Mesonet differences during Terra overpasses versus Aqua overpasses. This occurred in multiple different facets of the results. In tables 3.1-3.3, CERES-Terra had larger mean bias differences than CERES-Aqua by 6.31, 15.19, and 9.34 Wm^{-2} for 2019, 2020, and 2021, respectively. The RMS also was larger for CERES-Terra than CERES-Aqua but by only 1.72, 9.17, and 0.98 Wm^{-2} for the same three years. The pattern of larger MBD for CERES-Terra than CERES-Aqua continued for the higher cloud fraction bins, with approximately the same magnitudes of error as the clear-sky bins.

For the bi-sector correlation coefficient analysis, the correlations for all cloud fraction bins indicated a strong positive correlation. The separation between Terra and Aqua regarding the correlation with Mesonet was minimal for all three years and all cloud fraction bins, with the most significant difference in correlation being 0.02 for the 2019 and 2020 five to fifty percent cloud fraction bin. The bootstrapping analysis was done to determine if the cause of the relatively lower correlation of the less than one percent cloud fraction bin caused the lower sample size, which was the null hypothesis. All correlations lie well within the 95% confidence interval. Therefore, we

reject the null hypothesis, and the cause of the lower correlation in the smallest cloud fraction must be caused by something other than the sample size. Possible reasons for this will be explored later in the discussion.

There are more areas in 2019, 2020, and 2021 where CERES-Terra-Mesonet differences are larger than CERES-Aqua. In addition, CERES-Terra has larger magnitudes of differences than CERES-Aqua when both instruments' means are larger than the annual mean Mesonet irradiances.

In the climate division box-and-whisker plots, the median downward shortwave irradiances for all nine climate divisions were larger for Terra than Aqua. The differences between CERES-Terra and CERES-Aqua were uniformly about 15 Wm^{-2}. The offset appears not only with the medians but also with the quartiles and extrema.

4.1.2 Regional Aerosol and Cloud Climatology

Aerosol and cloud-effective radiative forcing have significant impacts on the climate. Clouds and aerosols both scatter and absorb shortwave solar radiation and can result in a net decrease in surface solar irradiance. CERES-Mesonet differences are usually positive, especially in all-sky conditions. The seasonal changes in aerosol and cloud properties could affect the CERES-Mesonet differences.

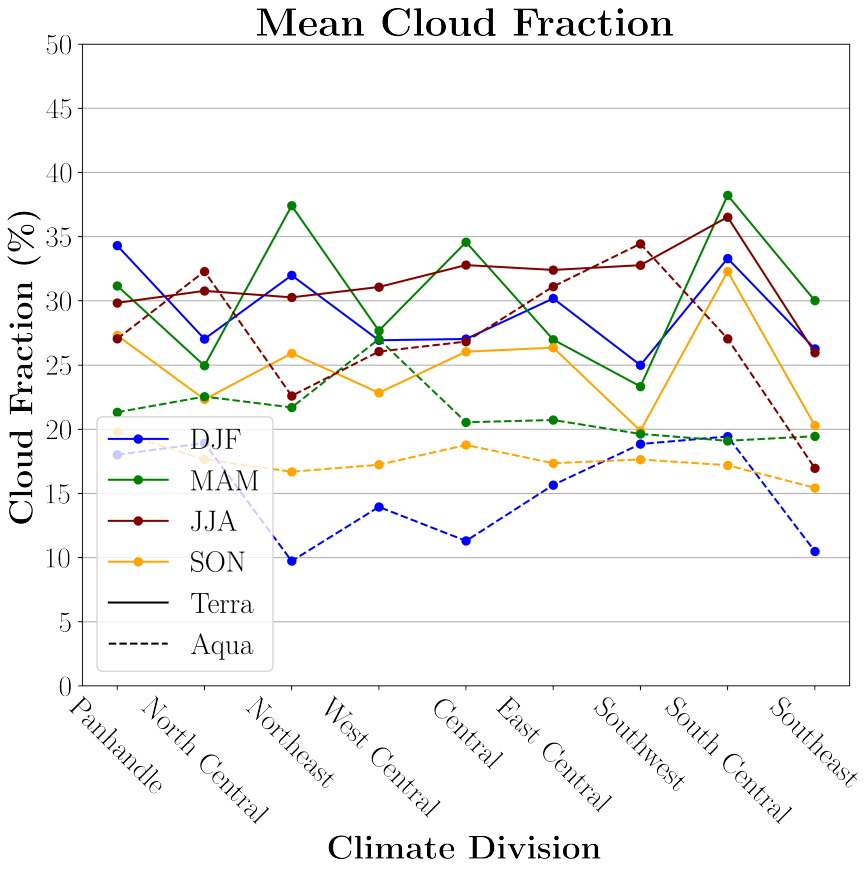

Figure 4.1: Mean cloud fraction for MODIS-Terra (solid lines) and MODIS-Aqua (dashed lines) (%) by climate division and winter (blue lines), spring (green lines), Summer (brown lines), and fall (orange lines) in 2019-2021.

Figure 4.1 shows the mean cloud fraction. This would have the largest impact on the all-sky data as the clear-sky data filters out cloud fractions greater than 5%. On average, the mean cloud fraction tends to be larger during Terra overpasses than Aqua. As a result, some of the larger CERES-Mesonet differences during Terra overpasses could be cloud-driven, even though the correlation between CERES-Terra and Mesonet in the larger cloud fraction bin is robust. Furthermore, there is also a seasonal dependence on the amount of cloud fraction. Generally, summers and springs have higher mean cloud fractions than other seasons. This could be a major reason

why the CERES-Mesonet differences for all-sky are much larger in the summertime than in other seasons and why the Summer CERES-Mesonet clear-sky differences are not very different from the other seasons.

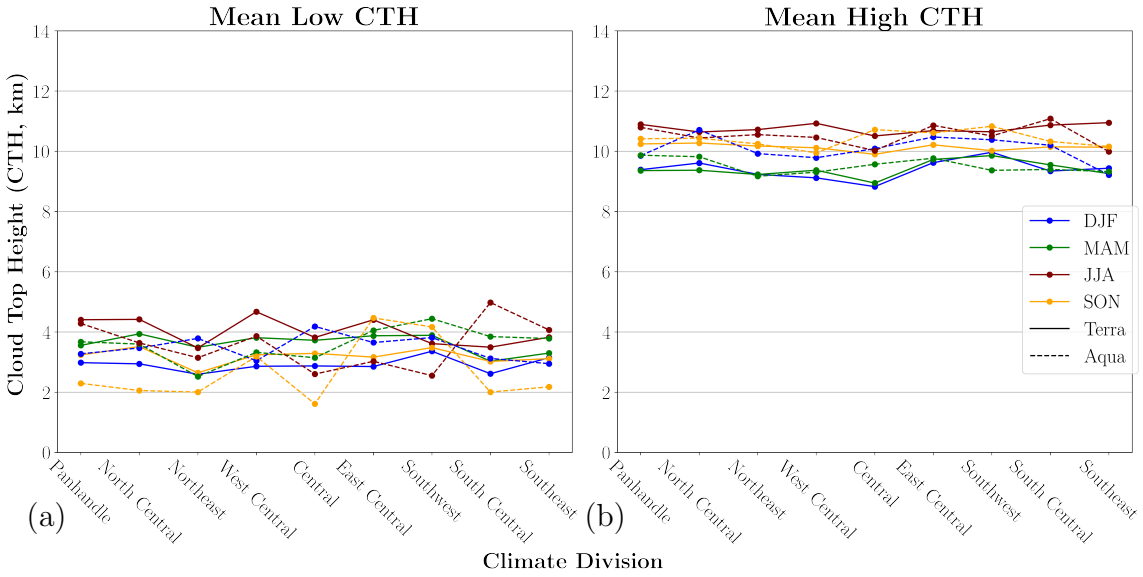

Figure 4.2: Mean cloud top height (CTH) for MODIS-Terra (solid lines) and MODIS-Aqua (dashed lines) (%) by climate division and winter (blue lines), spring (green lines), summer (brown lines), and fall (orange lines) in 2019-2021. (a) High clouds and (b) low clouds are considered.

The mean low and high cloud top heights indicate the cloud type. Cloud type is essential for this study because the type influences how much shortwave solar radiation is transmitted through the cloud. Cirrus clouds are optically thin, transmitting more solar radiation to the surface (Fu and Liou 1993). Even though there is less radiation attenuated by cirrus, the amount could still contribute to some of the CERES-Mesonet differences if the cirrus cloud fraction is not adequately accounted for in the parameterized CERES surface flux estimation scheme. Since cirrus scatter less radiation back into space, they are much harder to detect on passive remote sensors, even at near-infrared and infrared wavelengths. The high cloud top heights

have a strong seasonal dependence (Figure 4.2a). This is due to seasonal changes in the tropopause height. Warmer air causes the free troposphere to expand, and cooler air results in the free troposphere getting shallower (Chan and Wood 2013). For the low cloud top heights, the summer and spring tend to have the highest altitudes (Figure 4.2b). This is due to the increased frequency of cumuliform clouds in these seasons due to the more significant water vapor concentration and forcing for ascent. The winter and fall have lower cloud top heights due to the drier climate and more stable static stability. This results in less cumulus congestus clouds, which are more optically thick.

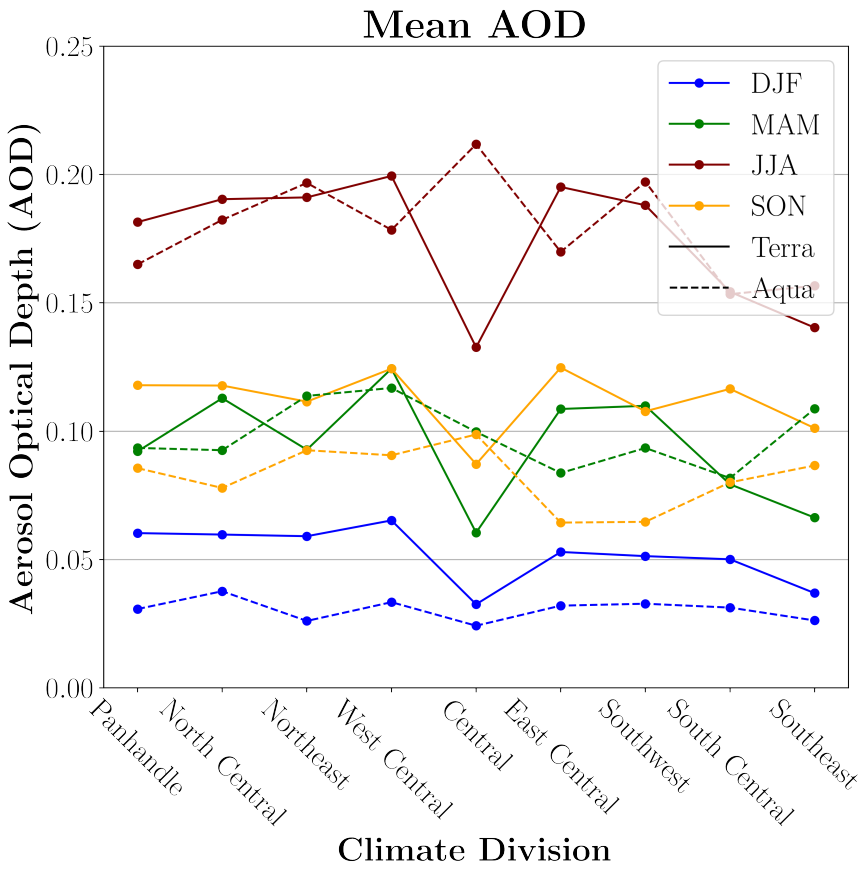

Figure 4.3: Mean aerosol optical depth (AOD) for MODIS-Terra (solid lines) and MODIS-Aqua (dashed lines) (%) by climate division and winter (blue lines), spring (green lines), summer (brown lines), and fall (orange lines) in 2019-2021.

According to Gui et al. (2021), aerosol optical depth (AOD) tends to be the largest in North America in the summer and the smallest in the winter. The AOD retrievals verified that AOD is largest in the Oklahoma summer and smallest in the winter, with an average difference of 0.13 between the two seasons (Figure 4.3). The fall and spring were similar in the mean aerosol optical depths for all three years. As a result, the summer is more likely to influence aerosol concentration and could explain the considerable CERES-Mesonet differences by changing the atmospheric transmittance term of the parameterization. However, the distribution of aerosol loading is spatially

heterogeneous and highly dependent on mesoscale sources, such as wildfires and dust (Chang et al. 2021). As a result, significant weather and climate events can drastically change the AOD every year.

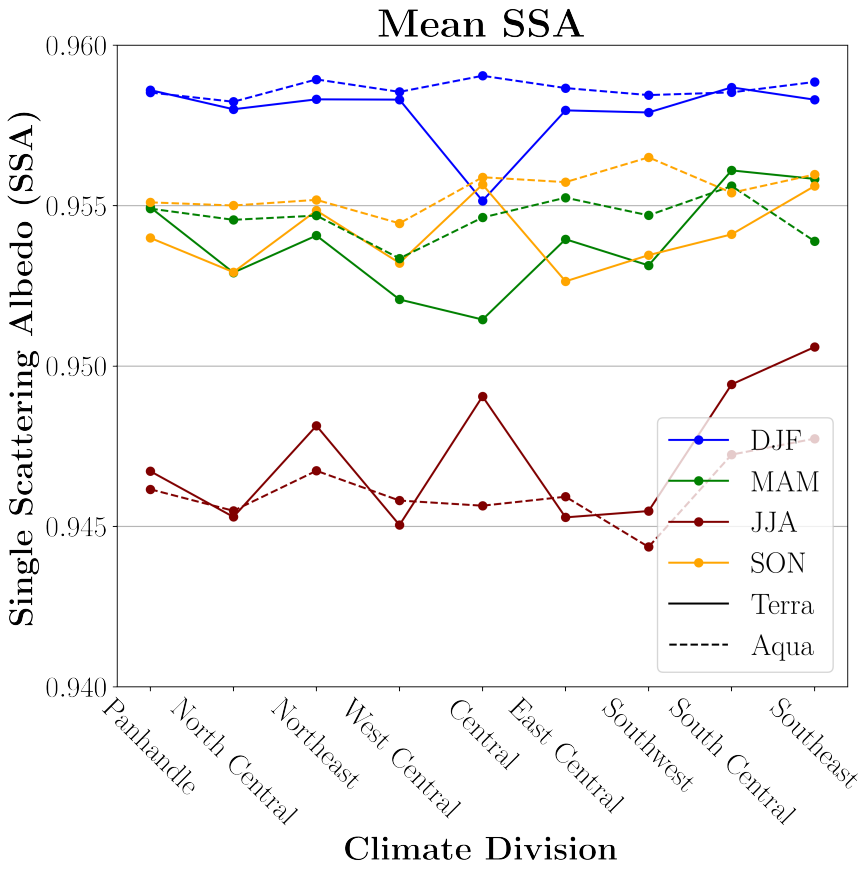

Figure 4.4: Mean single scattering albedo (SSA) for MODIS-Terra (solid lines) and MODIS-Aqua (dashed lines) (%) by climate division and winter (blue lines), spring (green lines), summer (brown lines), and fall (orange lines) in 2019-2021.

The single scattering albedo (SSA) is the ratio of the scattering coefficient to the extinction coefficient (Petty 2006). Therefore, SSA is a good measure of how much solar radiation is scattered by the atmosphere. SSA suggests the aerosol type. From 2019-2021, the SSA was lower in the summer than in the other three seasons (Figure 4.4). However, the differences between the summer and winter SSAs is only about

0.015. They are significantly smaller than the CERES-derived SSA product standard error. Therefore, the seasonal differences of SSA are insignificant, and we cannot draw any conclusions from the SSA.

4.1.3 Small Cloud Obstruction

One of the challenges with the CERES simple parameterized code is the calculation of cloud transmittance. The product uses cloud reflectance to estimate how much radiation is attenuated before reaching the surface. Still, isolated, small aerial clouds with large optical depths would drastically decrease the downward shortwave irradiance at that specific Mesonet station. However, since the CERES footprint is 20-50 km, the effects of small cumulus clouds are not seen in most of the footprint. Consequentially, the overall CERES measured downward shortwave radiative flux would be much larger than the Mesonet observed surface irradiance. The CERES measurement is from the TOA, and the algorithm only calculates the estimated cloud transmittance in the pixel. Since the Mesonet is a surface observation, an optically thick cumulus cloud directly over the pyranometer greatly reduces the surface irradiance. In addition, the frequency of these optically thick small cumuli is very seasonal dependant. Since the moisture content is climatologically larger in the summer, cloud nucleation and formation are more common (Yang et al. 2019). As a result, small cloud obstruction tends to be more of an influence with the comparison in the summer months.

4.1.4 Diffuse Radiative Transfer Effects

Another possible source of uncertainty is the diffuse radiation from clouds and multiple scattering. Previous work by Chakraborty and Lee (2021) discussed how CERES

struggled to estimate the diffuse component of solar radiation than the direct. This is due to the complicated nature of diffuse radiation. Diffuse radiation involves at least two plus orders of scattering (Petty 2006). Even after being reflected in the cloud, the light is scattered in multiple directions and can be scattered more by aerosols, gases, and other clouds. For example, on a typical summer day in Oklahoma, there might be dozens of fair weather cumuli in the CERES footprint.

In addition to clouds, surface reflectance also contributes to the diffuse component of shortwave solar radiation. The amount of surface reflection is dependent on the land surface. This is calculated using the Bi-directional Reflectance Function (BRDF) (Koepke et al. 1985). The BRDF formula is completely reliant on the land surface. Generally, the amount of radiation reflected from the surface is related to the surface albedo (Tang et al. 2006). Lighter surfaces, like fresh snow and sand, have higher albedos, which reflect more solar radiation at shorter wavelengths. Darker surfaces, such as pavement and forest, have lower albedos and reflect less radiation from the surface. As a result, Mesonet stations in the western portion of Oklahoma are more likely to have an increased diffuse radiation component from the land surface than the eastern portion of Oklahoma. Therefore, the diffuse component of solar radiation is likely larger in the western, less forested region of Oklahoma and likely contributes to some of the negative CERES-Mesonet differences.

In addition to surface reflection in the smaller wavelengths, there is surface emission in the longer wavelengths. While the primary goal of this study was to examine shortwave radiation, CERES considers wavelengths up to 5 μm as part of the shortwave band. Surface emission increases around 3 μm for sandy or desert surfaces and around 4 μm for urban areas (Tang et al. 2006). Conversely, there is little surface emission from forested land surfaces. Therefore, CERES is likely measuring some

longwave radiation from the surface in the 3-5 μm range in the central and western portions of the state, which would result in larger CERES-Mesonet differences. The eastern regions of the state are mostly forested, so there would be less contribution from surface emission there.

Currently, one of the best tools available for calculating the total downwelling shortwave radiation reaching the surface is the libRadtran radiative transfer model (Emde et al. 2016; Mayer and Kylling 2005). This model can simulate radiative transfer involving many layers of cloud and aerosol optical properties, effective radii, and customize the sensor wavelengths. Therefore, to understand the 3D radiative effects of clouds in Oklahoma, future work with libRadtran, local field campaigns with measured diffuse radiation, and additional modeling will be needed to resolve the 3D radiative effects.

4.1.5 Wavelength Dependence

One of the challenges of comparing CERES and Mesonet is that they have different spectral ranges. The CERES instrument measures 250-5000 nm, and the Mesonet Li-Cor LI-200R pyranometers measure 400-1100 nm. As a result, the spectral bands between 250-400 nm and 1100-5000 nm are not measured from the Mesonet measurements. Instead, the Li-Cor instruments are calibrated to provide irradiance "equivalents" to cover the entire solar spectral range. That is, out-of-Li-Cor-range spectral contributions are assumed to change in the same way that the in-range contributions vary. In that way, the smaller spectral range of the Li-Cor is accounted for in the calibration procedure, and uncertainties only arise when the out-of-band spectral contributions do not change proportionally to the in-band contributions. This is

possible in the presence of clouds and for changing solar zenith angles. To estimate this effect, we estimate below the out-of-Li-Cor-range contributions for different solar zenith angles and cloud properties using the LibRadTran radiative transfer model with a 250-4000 nm spectral range (Emde et al. 2016; Mayer and Kylling 2005).

To approximate the standard atmosphere, we made the following assumptions:

- A U.S. standard atmosphere for trace gas profiles.
- A default rural aerosol profile of 0-1.5 km in the boundary layer.
- An AOD of 0.1, applying the mean AOD in Figure 4.3.
- A cloud fraction of 25% using the mean cloud fraction in Figure 4.1.
- Liquid water clouds have an effective radius of 10 μm.
- Only low clouds, with a 0.7-1.0 km cloud layer.
- No ice water clouds.
- A Lambertian surface with a low spectral dependent albedo (Petty 2006).
- No surface emission (maximum wavelength of 4 μm).

We calculated the surface downward direct and diffuse irradiances with these assumptions for both the Mesonet and CERES wavelength ranges. Both spectral curves were integrated over all wavelengths as a function of cloud optical depth (COD) and solar zenith angle (SZA). Figure 4.6 shows the percentage of radiation not directly measured by Mesonet.

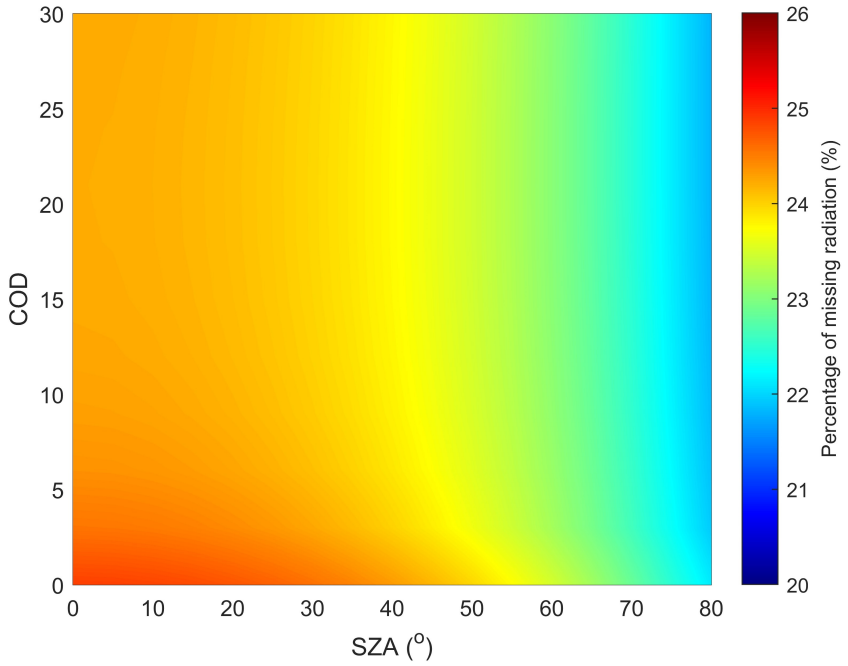

Figure 4.5: Percentage of solar irradiance not measured from Mesonet as a function of cloud optical depth (COD) and solar zenith angle (SZA), assuming a cloud fraction of 25% and an AOD of 0.1.

Table 4.1: LibRadtran approximate percentage of radiation not directly measured by Mesonet per season, solar zenith angle (SZA, June 21 and December 21), and cloud fraction (C.F.).

Season	**SZA**	**C.F.**	**Approx. Pct. of Radiation**
Summer	17.43°	0%	25%
Summer	17.43°	25%	24%
Winter	60.69°	0%	23%
Winter	60.69°	25%	22%

From Figure 4.5, the approximate percentage of radiation not directly measured from Mesonet was extracted (Table 4.1). The percent of solar radiation not directly measured in the winter decreases due to the higher solar zenith angle. The percentage

of unmeasured radiation is also higher for clear-sky cases because clouds and water vapor absorb much of the radiation in the 1100-5000 nm band, thereby minimizing the out-of-Li-Cor-range contributions to downwelling radiation. Without postprocessing or calibration of the Mesonet, the Mesonet would be lower than CERES by 200-250 Wm^{-2}. However, the Mesonet vs. CERES MBE is nowhere near that large in magnitude, with the seasonal mean maximum MBE being 38.15 Wm^{-2}.

Therefore, the CERES-Mesonet differences will decrease with cloud obstruction. Small cloud obstruction directly over the Mesonet site will cause a local increase in the CERES-Mesonet surface irradiance difference since the CERES footprint is too large to account for small clouds properly. Contrarily, CERES will be lower Mesonet in the presence of nearby convection due to not correctly accounting for the diffuse component of solar radiation. In addition, the percentage of unmeasured radiation decreases with the presence of clouds, which will cause the Mesonet to be overly corrected.

4.2 Broader Impacts and Future Work

This study was a regional assessment of the CERES-derived surface radiation product using a densely populated network of well-calibrated surface radiometers in multiple regional climate regimes. Due to the diversity of climate regimes in Oklahoma, the results found regionally in Oklahoma may apply to other areas with similar climates. This work has also been shared with Dr. Sajo Kato at NASA Langley and Dr. Brad Illston at the Oklahoma Mesonet so that they can identify potential areas of improvement with their radiation products. Furthermore, these estimates are crucial tests of our ability to study Earth's surface radiation budget from space with critical

links to dynamics and the hydrologic cycle. The hydrologic cycle is essential to the Earth's system as it drives convection and other latent heat processes.

To examine how our understanding of the overall climate system changes based on the CERES-Mesonet comparison, the study needs to be extended beyond three years. A multidecadal study could help infer regional changes in the radiation budget, which could be later applied globally. Global dimming and brightening are the long-term decrease or increases in the downward shortwave surface radiative fluxes (Wild 2009). This analysis will use CERES Energy Balanced and Filled (EBAF) Ed4.2 and Clouds and Radiative Swath (CRS) Ed4 products for long-term analysis and spatial variability, respectively (Kato et al. 2018; Scott et al. 2022). These are based on the more complex Fu-Liou radiative transfer model instead of a simple parameterized code (Fu and Liou 1993). These changes will be studied by climate division, and other beneficial meteorological and geographical properties, such as rainfall frequency and topography, will be explored. In addition, future work will examine 3D cloud and radiative properties using the Multi-angle Image Spectrometer (MISR) and CloudSat W-Band Radar. These observations will be used for understanding the fractal geometry of smaller clouds and, to some extent, the 3-D structure of larger clouds, which will help scientists understand their radiative properties. Radiation closure studies will need to be applied to understand the causality of the differences. CloudSat W-band radar will provide vertically resolved cloud properties. When included in Global Climate Models, these findings enable new climate assessments, helping policymakers evaluate future climate mitigation efforts. In addition, data from the Small-Scale Variability of Solar Radiation (SV2SR) field campaign at Atmospheric Radiation Measurement (ARM) Southern Great Plains (SGP) in Summer 2023 may

be used to evaluate small-scale variability in the surface radiation budget. In addition, the relationships between aerosol and cloud properties discussed earlier and libRadtran will be further explored, informed by the atmospheric composition derived from the collocated satellite sensors (Emde et al. 2016). In addition, ice water clouds will need to be accounted for, given Oklahoma's large percentage of ice water clouds (Chiu et al. 2012).

Chapter 5

Conclusion

Overall, the key findings are that the more considerable CERES-Mesonet differences are during the Terra overpasses versus the Aqua overpasses. Unlike our results, Kratz et al. (2020) found similar bias between Terra and Aqua in their comparison over continents. Additionally, Scott et al. (2022) RMS values for both all-sky and clear-sky are significantly larger than in our study. Both Scott et al. (2022) and Kratz et al. (2020) show that all-sky irradiances have higher RMS and MBD than clear-sky irradiances over continents. However, the CERES-station difference in Scott et al. (2022) is only 4 Wm^{-2}. This study found little difference in the RMS and correlation coefficients between the three cloud fraction bins. However, there is a difference between the all-sky and clear-sky seasonal analyses. It is quite likely that since the largest bin of the non-bi-squared regression analysis is 50% cloud fraction, much of the higher CERES-Mesonet differences lie with cloud fractions greater than 50%. The systematic larger Terra CERES-Mesonet differences than Aqua were not expected. A possible explanation for the larger CERES-Mesonet differences during Terra could be high-level cirrus, which MODIS struggles to detect and is often indistinguishable from dust (Roskovensky and Liou 2005).

The southeast region of Oklahoma has the largest distribution of irradiance differences. This is possibly due to water vapor feedbacks and higher annual mean cloud fraction. In addition, the Mesonet station density is smaller in the southeast region,

which could have influenced the larger standard deviations, RMS, and MBD. Before the spatial analysis, we expected the southeast region to have the largest RMS and MBD, so our results were unsurprising. In addition, the southwest region has a high frequency of thunderstorm days per year.

The spring and summer had the highest CERES-Mesonet differences. Possible explanations for the larger decrease in correlations in these seasons are increases in overall cloud fraction and aerosol optical depth during spring and summer. The late spring and summer also feature more deep convective clouds. These clouds are more optically thick, have larger cloud top heights, and are more likely to scatter diffuse shortwave radiation, which CERES is less likely to resolve (Chakraborty et al. 2022). The fall and winter seasons have a relatively good agreement for all-sky and clear-sky days. This mirrors our expectation as the three-dimensional fractal nature of convective clouds is difficult to account for in a simple parameterization.

This work will be helpful to apply elsewhere globally with similar climate regimes. Additionally, we learned that the simple parameterization performs well in clear-sky environments and decently in all-sky environments. As a result, the CERES product is a great product to estimate the surface radiation budget on cloud-free days and cloudy days in the fall and winter, when cloud transmittance can be more easily assessed. Future upgrades to the CERES product will use the Fu-Liou radiative transfer model, which will help resolve the three-dimensional radiative effects of convective clouds. Improving our understanding of the surface radiation budget will help us improve existing global climate models to more accurately model climate change.

References

Ahrens, C. D., 2016: *Meteorology Today: An Introduction to Weather, Climate, and the Environment*. Eleventh edition/student edition ed., Cengage Learning, Boston.

Brock, F. V., K. C. Crawford, R. L. Elliott, G. W. Cuperus, S. J. Stadler, H. L. Johnson, and M. D. Eilts, 1995: The Oklahoma Mesonet: A Technical Overview. *Journal of Atmospheric and Oceanic Technology*, **12 (1)**, 5–19, https://doi.org/10.1175/1520-0426(1995)012⟨0005:TOMATO⟩2.0.CO;2, URL http://journals.ametsoc.org/doi/10.1175/1520-0426(1995)012⟨0005:TOMATO⟩2.0.CO;2.

Brown, P. T., W. Li, L. Li, and Y. Ming, 2014: Top-of-atmosphere radiative contribution to unforced decadal global temperature variability in climate models. *Geophysical Research Letters*, **41 (14)**, 5175–5183, https://doi.org/10.1002/2014GL060625, URL http://doi.wiley.com/10.1002/2014GL060625.

Budyko, M. I., 1969: The effect of solar radiation variations on the climate of the Earth. *Tellus*, **21 (5)**, 611–619, https://doi.org/10.1111/j.2153-3490.1969.tb00466.x, URL http://tellusa.net/index.php/tellusa/article/view/10109.

Chai, T., and R. R. Draxler, 2014: Root mean square error (RMSE) or mean absolute error (MAE)? preprint, Numerical Methods. https://doi.org/10.5194/gmdd-7-1525-2014, URL https://gmd.copernicus.org/preprints/7/1525/2014/gmdd-7-1525-2014.pdf.

Chakraborty, T., and X. Lee, 2021: Large Differences in Diffuse Solar Radiation Among Current-Generation Reanalysis and Satellite-Derived Products. *Journal of Climate*, 1–52, https://doi.org/10.1175/JCLI-D-20-0979.1, URL https://journals.ametsoc.org/view/journals/clim/aop/JCLI-D-20-0979.1/JCLI-D-20-0979.1.xml.

Chakraborty, T., X. Lee, and D. M. Lawrence, 2022: Diffuse Radiation Forcing Constraints on Gross Primary Productivity and Global Terrestrial Evapotranspiration. *Earth's Future*, **10 (8)**, https://doi.org/10.1029/2022EF002805, URL https://onlinelibrary.wiley.com/doi/10.1029/2022EF002805.

Chan, K. M., and R. Wood, 2013: The seasonal cycle of planetary boundary layer depth determined using COSMIC radio occultation data: SEASONAL CYCLE OF PBL DEPTH. *Journal of Geophysical Research: Atmospheres*, **118 (22)**, 12,422–12,434, https://doi.org/10.1002/2013JD020147, URL http://doi.wiley.com/10.1002/2013JD020147.

Chang, I., and Coauthors, 2021: Spatiotemporal Heterogeneity of Aerosol and Cloud Properties Over the Southeast Atlantic: An Observational Analysis. *Geophysical Research Letters*, **48 (7)**, https://doi.org/10.1029/2020GL091469, URL https://onlinelibrary.wiley.com/doi/10.1029/2020GL091469.

Chiu, J. C., and Coauthors, 2012: Cloud droplet size and liquid water path retrievals from zenith radiance measurements: examples from the Atmospheric Radiation Measurement Program and the Aerosol Robotic Network. *Atmospheric Chemistry and Physics*, **12 (21)**, 10 313–10 329, https://doi.org/10.5194/acp-12-10313-2012, URL https://acp.copernicus.org/articles/12/10313/2012/.

Chopde, N. R., and M. M. K. Nichat, 2013: Landmark Based Shortest Path Detection by Using A* and Haversine Formula. *International Journal of Innovative Research in Computer and Communication Engineering*, **1 (2)**, 6, https://doi.org/https://doi.org/10.17762/ijritcc.v6i7.1690.

Chung, E.-S., and B. J. Soden, 2015: An Assessment of Direct Radiative Forcing, Radiative Adjustments, and Radiative Feedbacks in Coupled Ocean–Atmosphere Models*. *Journal of Climate*, **28 (10)**, 4152–4170, https://doi.org/10.1175/JCLI-D-14-00436.1, URL http://journals.ametsoc.org/doi/10.1175/JCLI-D-14-00436.1.

Darnell, W. L., W. F. Staylor, S. K. Gupta, N. A. Ritchey, and A. C. Wilber, 1992: Seasonal variation of surface radiation budget derived from International Satellite Cloud Climatology Project C1 data. *Journal of Geophysical Research*, **97 (D14)**, 15 741, https://doi.org/10.1029/92JD00675, URL http://doi.wiley.com/10.1029/92JD00675.

Dewitz, J., 2021: National Land Cover Database (NLCD) 2019 Products. U.S. Geological Survey, URL https://www.sciencebase.gov/catalog/item/5f21cef582cef313ed940043, https://doi.org/10.5066/P9KZCM54.

Efron, B., 1979: Bootstrap Methods: Another Look at the Jackknife. *The Annals of Statistics*, **7 (1)**, https://doi.org/10.1214/aos/1176344552, URL https://projecteuclid.org/journals/annals-of-statistics/volume-7/issue-1/Bootstrap-Methods-Another-Look-at-the-Jackknife/10.1214/aos/1176344552.full.

Emde, C., and Coauthors, 2016: The libRadtran software package for radiative transfer calculations (version 2.0.1). *Geoscientific Model Development*, **9 (5)**, 1647–1672, https://doi.org/10.5194/gmd-9-1647-2016, URL https://gmd.copernicus.org/articles/9/1647/2016/.

Ensor, D. S., W. M. Porch, M. J. Pilat, and R. J. Charlson, 1971: Influence of the Atmospheric Aerosol on Albedo. *Journal of Applied Meteorology*,

10 (6), 1303–1306, https://doi.org/10.1175/1520-0450(1971)010⟨1303:IOTAAO⟩2.0.CO;2, URL http://journals.ametsoc.org/doi/10.1175/1520-0450(1971)010⟨1303:IOTAAO⟩2.0.CO;2.

Forster, P. M., and Coauthors, 2021: The Earth's Energy Budget, Climate Feedbacks and Climate Sensitivity. *Climate Change 2021: The Physical Science Basis. Contribution of Working Group I to the Sixth Assessment Report of the Intergovernmental Panel on Climate Change*, 923–1054, https://doi.org/10.1017/9781009157896.009.

Fu, Q., and K. N. Liou, 1993: Parameterization of the Radiative Properties of Cirrus Clouds. *Journal of the Atmospheric Sciences*, **50 (13)**, 2008–2025, https://doi.org/10.1175/1520-0469(1993)050⟨2008:POTRPO⟩2.0.CO;2, URL https://journals.ametsoc.org/view/journals/atsc/50/13/1520-0469_1993_050_2008_potrpo_2_0_co_2.xml?tab_body=abstract-display.

Goody, R. M., and Y. L. Yung, 1995: *Atmospheric Radiation: Theoretical Basis*. 2nd ed., Oxford Univ. Press, New York.

Gui, K., and Coauthors, 2021: Seasonal variability and trends in global type-segregated aerosol optical depth as revealed by MISR satellite observations. *Science of The Total Environment*, **787**, 147 543, https://doi.org/10.1016/j.scitotenv.2021.147543, URL https://linkinghub.elsevier.com/retrieve/pii/S0048969721026140.

Guttman, N. B., and R. G. Quayle, 1996: A Historical Perspective of U.S. Climate Divisions. *Bulletin of the American Meteorological Society*, **77 (2)**, 293–303, https://doi.org/10.1175/1520-0477(1996)077⟨0293:AHPOUC⟩2.0.CO;2, URL http://journals.ametsoc.org/doi/10.1175/1520-0477(1996)077⟨0293:AHPOUC⟩2.0.CO;2.

Hartmann, D. L., 2016: *Global Physical Climatology*. Second edition ed., Elsevier, Amsterdam ; Boston.

Illston, B. G., J. B. Basara, and K. C. Crawford, 2004: Seasonal to interannual variations of soil moisture measured in Oklahoma. *International Journal of Climatology*, **24 (15)**, 1883–1896, https://doi.org/10.1002/joc.1077, URL https://onlinelibrary.wiley.com/doi/10.1002/joc.1077.

Isaac, E., 2018: Test for Significance of Pearson's Correlation Coefficient ( ). *International Journal of Innovative Mathematics, Statistics & Energy Policies*, 13.

Kato, S., N. G. Loeb, F. G. Rose, D. R. Doelling, D. A. Rutan, T. E. Caldwell, L. Yu, and R. A. Weller, 2013: Surface Irradiances Consistent with CERES-Derived Top-of-Atmosphere Shortwave and Longwave Irradiances. *Journal of Climate*, **26 (9)**, 2719–2740, https://doi.org/10.1175/JCLI-D-12-00436.1, URL http://journals.ametsoc.org/doi/10.1175/JCLI-D-12-00436.1.

Kato, S., and Coauthors, 2018: Surface Irradiances of Edition 4.0 Clouds and the Earth's Radiant Energy System (CERES) Energy Balanced and Filled (EBAF) Data Product. *Journal of Climate*, **31 (11)**, 4501–4527, https://doi.org/10.1175/JCLI-D-17-0523.1, URL http://journals.ametsoc.org/doi/10.1175/JCLI-D-17-0523.1.

Koepke, P., K. Kriebel, and B. Dietrich, 1985: The effect of surface reflection function and of atmospheric parameters on the shortwave radiation budget. *Advances in Space Research*, **5 (6)**, 351–354, https://doi.org/10.1016/0273-1177(85)90340-0, URL https://linkinghub.elsevier.com/retrieve/pii/0273117785903400.

Kratz, D. P., S. K. Gupta, A. C. Wilber, and V. E. Sothcott, 2010: Validation of the CERES Edition 2B Surface-Only Flux Algorithms. *Journal of Applied Meteorology and Climatology*, **49 (1)**, 164–180, https://doi.org/10.1175/2009JAMC2246.1, URL http://journals.ametsoc.org/doi/10.1175/2009JAMC2246.1.

Kratz, D. P., S. K. Gupta, A. C. Wilber, and V. E. Sothcott, 2020: Validation of the CERES Edition-4A Surface-Only Flux Algorithms. *Journal of Applied Meteorology and Climatology*, **59 (2)**, 281–295, https://doi.org/10.1175/JAMC-D-19-0068.1, URL https://journals.ametsoc.org/view/journals/apme/59/2/jamc-d-19-0068.1.xml.

Lenhardt, E., J. Redemann, F. Xu, C. Homeyer, and L. Gao, 2021: Relationships Between Lidar Aerosol Extinction and Backscatter Coefficients with CCN Number Concentrations in the Southeast Atlantic. M.S. thesis, University of Oklahoma, Norman.

Lenhardt, E. D., and Coauthors, 2023: Use of lidar aerosol extinction and backscatter coefficients to estimate cloud condensation nuclei (CCN) concentrations in the southeast Atlantic. *Atmospheric Measurement Techniques*, **16 (7)**, 2037–2054, https://doi.org/10.5194/amt-16-2037-2023, URL https://amt.copernicus.org/articles/16/2037/2023/.

Loeb, N., N. Manalo-Smith, W. Su, M. Shankar, and S. Thomas, 2016: CERES Top-of-Atmosphere Earth Radiation Budget Climate Data Record: Accounting for in-Orbit Changes in Instrument Calibration. *Remote Sensing*, **8 (3)**, 182, https://doi.org/10.3390/rs8030182, URL http://www.mdpi.com/2072-4292/8/3/182.

Lohmann, U., and J. Feichter, 2005: Global indirect aerosol effects: a review. *Atmos. Chem. Phys.*

Mayer, B., and A. Kylling, 2005: Technical note: The libRadtran software package for radiative transfer calculations – description and examples of use. *Atmos. Chem. Phys.*

McCree, K. J., 2022: Light Measurement. LI-COR.

McPherson, R. A., and Coauthors, 2007: Statewide Monitoring of the Mesoscale Environment: A Technical Update on the Oklahoma Mesonet. *Journal of Atmospheric and Oceanic Technology*, **24 (3)**, 301–321, https://doi.org/10.1175/JTECH1976.1, URL http://journals.ametsoc.org/doi/10.1175/JTECH1976.1.

Petty, G. W., 2006: *A First Course in Atmospheric Radiation*. 2nd ed., Sundog Pub, Madison.

Ramanathan, V., P. J. Crutzen, J. T. Kiehl, and D. Rosenfeld, 2001: Aerosols, Climate, and the Hydrological Cycle. *Science*, **294 (5549)**, 2119–2124, https://doi.org/10.1126/science.1064034, URL https://www.science.org/doi/10.1126/science.1064034.

Redemann, J., and Coauthors, 2021: An overview of the ORACLES (ObseRvations of Aerosols above CLouds and their intEractionS) project: aerosol–cloud–radiation interactions in the southeast Atlantic basin. *Atmospheric Chemistry and Physics*, **21 (3)**, 1507–1563, https://doi.org/10.5194/acp-21-1507-2021, URL https://acp.copernicus.org/articles/21/1507/2021/.

Roskovensky, J. K., and K. N. Liou, 2005: Differentiating airborne dust from cirrus clouds using MODIS data: DETECTING DUST AND CIRRUS FROM SPACE. *Geophysical Research Letters*, **32 (12)**, n/a–n/a, https://doi.org/10.1029/2005GL022798, URL http://doi.wiley.com/10.1029/2005GL022798.

Schober, P., C. Boer, and L. A. Schwarte, 2018: Correlation Coefficients: Appropriate Use and Interpretation. *Anesthesia & Analgesia*, **126 (5)**, 1763–1768, https://doi.org/10.1213/ANE.0000000000002864, URL http://journals.lww.com/00000539-201805000-00050.

Schwertman, N. C., M. A. Owens, and R. Adnan, 2004: A simple more general boxplot method for identifying outliers. *Computational Statistics & Data Analysis*, **47 (1)**, 165–174, https://doi.org/10.1016/j.csda.2003.10.012, URL https://linkinghub.elsevier.com/retrieve/pii/S0167947303002469.

Scott, H. D., and Coauthors, 2000: Water and Chemical Transport in Soils of the Southeastern USA. *Southern Cooperative Series Bulletin*.

Scott, R. C., and Coauthors, 2022: Clouds and the Earth's Radiant Energy System (CERES) Cloud Radiative Swath (CRS) Edition 4 Data Product. *Journal of Atmospheric and Oceanic Technology*, **39 (11)**, 1781–1797, https://doi.org/10.1175/JTECH-D-22-0021.1, URL https://journals.ametsoc.org/view/journals/atot/39/11/JTECH-D-22-0021.1.xml.

Shafer, M. A., C. A. Fiebrich, D. S. Arndt, S. E. Fredrickson, and T. W. Hughes, 2000: Quality Assurance Procedures in the Oklahoma Mesonetwork. *Journal of Atmospheric and Oceanic Technology*, **17 (4)**, 474–494, https://doi.org/10.1175/1520-0426(2000)017⟨0474:QAPITO⟩2.0.CO;2, URL http://journals.ametsoc.org/doi/10.1175/1520-0426(2000)017⟨0474:QAPITO⟩2.0.CO;2.

Smith, C. J., and Coauthors, 2018: Understanding Rapid Adjustments to Diverse Forcing Agents. *Geophysical Research Letters*, **45 (21)**, https://doi.org/10.1029/2018GL079826, URL https://onlinelibrary.wiley.com/doi/10.1029/2018GL079826.

Stocker, T. F., and Coauthors, 2013: IPCC, 2013. *Climate Change 2013: The Physical Science Basis. Contribution of Working Group I to the Fifth Assessment Report of the Intergovernmental Panel on Climate Change*.

Tang, B., Z.-L. Li, and R. Zhang, 2006: A direct method for estimating net surface shortwave radiation from MODIS data. *Remote Sensing of Environment*, **103 (1)**, 115–126, https://doi.org/10.1016/j.rse.2006.04.008, URL https://linkinghub.elsevier.com/retrieve/pii/S0034425706001532.

Twomey, S., 1959: The nuclei of natural cloud formation part I: The chemical diffusion method and its application to atmospheric nuclei. *Geofisica Pura e Applicata*, **43 (1)**, 227–242, https://doi.org/10.1007/BF01993559, URL http://link.springer.com/10.1007/BF01993559.

Wallace, J. M., and P. V. Hobbs, 2006: *Atmospheric Science: An Introductory Survey*. 2nd ed., No. v. 92, International geophysics series, Elsevier Academic Press, Amsterdam ; Boston, oCLC: ocm62421169.

Wielicki, B. A., B. R. Barkstrom, E. F. Harrison, R. B. Lee, G. Louis Smith, and J. E. Cooper, 1996: Clouds and the Earth's Radiant Energy System (CERES): An Earth Observing System Experiment. *Bulletin of the American Meteorological Society*, **77 (5)**, 853–868, https://doi.org/10.1175/1520-0477(1996)077⟨0853:CATERE⟩2.0.CO;2, URL http://journals.ametsoc.org/doi/10.1175/1520-0477(1996)077⟨0853:CATERE⟩2.0.CO;2.

Wild, M., 2009: Global dimming and brightening: A review. 31, https://doi.org/0148-0227/09/2008JD011470.

Wild, M., and Coauthors, 2015: The energy balance over land and oceans: an assessment based on direct observations and CMIP5 climate models. *Climate Dynamics*, **44 (11-12)**, 3393–3429, https://doi.org/10.1007/s00382-014-2430-z, URL http://link.springer.com/10.1007/s00382-014-2430-z.

Xie, Y., and Y. Liu, 2013: A new approach for simultaneously retrieving cloud albedo and cloud fraction from surface-based shortwave radiation measurements. *Environmental Research Letters*, **8 (4)**, 044 023, https://doi.org/10.1088/1748-9326/8/4/044023, URL https://iopscience.iop.org/article/10.1088/1748-9326/8/4/044023.

Yang, Y., and Coauthors, 2019: Toward understanding the process-level impacts of aerosols on microphysical properties of shallow cumulus cloud using aircraft observations. *Atmospheric Research*, **221**, 27–33, https://doi.org/10.1016/j.atmosres.2019.01.027, URL https://linkinghub.elsevier.com/retrieve/pii/S0169809518311773.

Zhang, X., and M. Nearing, 2005: Impact of climate change on soil erosion, runoff, and wheat productivity in central Oklahoma. *CATENA*, **61 (2-3)**, 185–195, https://doi.org/10.1016/j.catena.2005.03.009, URL https://linkinghub.elsevier.com/retrieve/pii/S0341816205000494.